First Year *Wilkinson Microwave Anisotropy Probe* (*WMAP*[1]) Observations: Preliminary Maps and Basic Results

C. L. Bennett[2], M. Halpern[3], G. Hinshaw[2], N. Jarosik[4], A. Kogut[2], M. Limon[2,5], S. S. Meyer[6], L. Page[4], D. N. Spergel[7], G. S. Tucker[2,5,8], E. Wollack[2], E. L. Wright[9], C. Barnes[4], M. R. Greason[10], R. S. Hill[10], E. Komatsu[7], M. R. Nolta[4], N. Odegard[10], H. V. Peiris[7], L. Verde[7], J. L. Weiland[10]

Charles.L.Bennett@NASA.gov

ABSTRACT

We present full sky microwave maps in five frequency bands (23 to 94 GHz) from the *WMAP* first year sky survey. Calibration errors are <0.5% and the low systematic error level is well specified. The cosmic microwave background (CMB) is separated from the foregrounds using multifrequency data. The sky maps are consistent with the 7° full-width at half-maximum (FWHM) *Cosmic Background Explorer (COBE)* maps. We report more precise, but consistent, dipole and quadrupole values.

The CMB anisotropy obeys Gaussian statistics with $-58 < f_{NL} < 134$ (95% CL). The $2 \leq l \leq 900$ anisotropy power spectrum is cosmic variance limited for $l < 354$ with a signal-to-noise ratio >1 per mode to $l = 658$. The temperature-polarization cross-power spectrum reveals both acoustic features and a large angle correlation from reionization. The optical depth of reionization is $\tau = 0.17 \pm 0.04$, which implies a reionization epoch of $t_r = 180^{+220}_{-80}$ Myr (95% CL) after the Big Bang at a redshift of $z_r = 20^{+10}_{-9}$ (95% CL) for a range of ionization scenarios. This early reionization is incompatible with the presence of a significant warm dark matter density.

A best-fit cosmological model to the CMB and other measures of large scale structure works remarkably well with only a few parameters. The age of the best-fit universe is $t_0 = 13.7 \pm 0.2$ Gyr old. Decoupling was $t_{dec} = 379^{+8}_{-7}$ kyr after the Big Bang at a redshift of $z_{dec} = 1089 \pm 1$. The thickness of the decoupling surface was $\Delta z_{dec} = 195 \pm 2$. The matter density of the universe is $\Omega_m h^2 = 0.135^{+0.008}_{-0.009}$, the baryon density is $\Omega_b h^2 = 0.0224 \pm 0.0009$, and the total mass-energy of the universe is $\Omega_{tot} = 1.02 \pm 0.02$. There is progressively less fluctuation power on smaller scales, from *WMAP* to fine scale CMB measurements to galaxies and finally to the Ly-α forest. This is accounted for with a running spectral index, significant at the $\sim 2\sigma$ level. The spectral index of scalar fluctuations is fit as $n_s = 0.93 \pm 0.03$ at wavenumber $k_0 = 0.05$ Mpc^{-1} ($l_{eff} \approx 700$), with a slope of $dn_s/d\ln k = -0.031^{+0.016}_{-0.018}$ in the best-fit model. This flat

---

[1] *WMAP* is the result of a partnership between Princeton University and NASA's Goddard Space Flight Center. Scientific guidance is provided by the *WMAP* Science Team.

[2] Code 685, Goddard Space Flight Center, Greenbelt, MD 20771

[3] Dept. of Physics and Astronomy, University of British Columbia, Vancouver, BC Canada V6T 1Z1

[4] Dept. of Physics, Jadwin Hall, Princeton, NJ 08544

[5] National Research Council (NRC) Fellow

[6] Depts. of Astrophysics and Physics, EFI and CfCP, University of Chicago, Chicago, IL 60637

[7] Dept of Astrophysical Sciences, Princeton University, Princeton, NJ 08544

[8] Dept. of Physics, Brown University, Providence, RI 02912

[9] UCLA Astronomy, PO Box 951562, Los Angeles, CA 90095-1562

[10] Science Systems and Applications, Inc. (SSAI), 10210 Greenbelt Road, Suite 600 Lanham, Maryland 20706

universe model is composed of 4.4% baryons, 22% dark matter and 73% dark energy. The dark energy equation of state is limited to $w < -0.78$ (95% CL).

Inflation theory is supported with $n_s \approx 1$, $\Omega_{tot} \approx 1$, Gaussian random phases of the CMB anisotropy, and superhorizon fluctuations implied by the TE anticorrelations at decoupling. An admixture of isocurvature modes does not improve the fit. The tensor-to-scalar ratio is $r(k_0 = 0.002\ \mathrm{Mpc}^{-1}) < 0.71$ (95% CL). The lack of CMB fluctuation power on the largest angular scales reported by *COBE* and confirmed by *WMAP* is intriguing. *WMAP* continues to operate, so results will improve.

Subject headings: cosmic microwave background, cosmology: observations, early universe, dark matter, space vehicles, space vehicles: instruments, instrumentation: detectors, telescopes

1. INTRODUCTION

The cosmic microwave background (CMB) radiation was first detected by Penzias & Wilson (1965). After its discovery, a small number of experimentalists worked for years to better characterize the CMB as they searched for temperature fluctuations. A leader of this effort, and of the *WMAP* effort, was our recently deceased colleague, Professor David T. Wilkinson of Princeton University. He was also a leading member of the *Cosmic Background Explorer (COBE)* mission team, which accurately characterized the spectrum of the CMB (Mather et al. 1990, 1999) and first discovered anisotropy (Smoot et al. 1992; Bennett et al. 1992; Kogut et al. 1992; Wright et al. 1992). The *MAP* was recently renamed *WMAP* in his honor.

The general recognition that the CMB is a primary tool for determining the global properties, content, and history of the universe has led to the tremendous interest and growth of the field. In addition to the characterization of the large-scale anisotropy results from *COBE* (Bennett et al. 1996; Hinshaw et al. 1996a,b; Kogut et al. 1996b,c,a; Górski et al. 1996; Wright et al. 1996a), a host of experiments have measured the finer scale anisotropy (Benoit et al. 2003; Grainge et al. 2003; Pearson et al. 2002; Ruhl et al. 2003; Kuo et al. 2002; Dawson et al. 2001; Halverson et al. 2002; Hanany et al. 2000; Leitch et al. 2000; Wilson et al. 2000; Padin et al. 2001; Romeo et al. 2001; Harrison et al. 2000; Peterson et al. 2000; Baker et al. 1999; Coble et al. 1999; Dicker et al. 1999; Miller et al. 1999; de Oliverira-Costa et al. 1998; Cheng et al. 1997; Hancock et al. 1997; Netterfield et al. 1997; Piccirillo et al. 1997; Tucker et al. 1997; Gundersen et al. 1995; de Bernardis et al. 1994; Ganga et al. 1993; Myers et al. 1993; Tucker et al. 1993). As a result of these tremendous efforts, the first acoustic peak of the anisotropy power spectrum has been unambiguously detected (Knox & Page 2000; Mauskopf et al. 2000; Miller et al. 1999) and CMB observations have placed important constraints on cosmological models. Recently, Kovac et al. (2002) reported the first detection of CMB polarization arising from the anisotropic scattering of CMB photons at decoupling, ushering in a new era of CMB polarization measurements.

The *WMAP* mission was designed to advance observational cosmology by making full sky CMB maps with accuracy, precision, and reliability, as described by Bennett et al. (2003a). The instrument observes the temperature difference between two directions (as did *COBE*) using two nearly identical sets of optics (Page et al. 2003c,a). These optics focus radiation into horns (Barnes et al. 2002) that feed differential microwave radiometers (Jarosik et al. 2003a). We produce full sky maps in five frequency bands from the radiometer data of temperature differences measured over the full sky. A CMB map is the most compact representation of CMB anisotropy without loss of information.

In this paper we present the maps, their properties, and a synopsis of the basic results of the first-year of observations. In §2 we give a brief overview of the *WMAP* mission. In §3 we summarize the data analysis, calibration, and systematic errors of the experiment, which are discussed in much greater detail in the companion papers by Hinshaw et al. (2003a), Page et al. (2003a), Jarosik et al. (2003b), and Barnes et al. (2003). In §4 we present the maps and their

sampling properties, and we compare the *WMAP* and *COBE* maps. In §5 we summarize the foreground analyses of Bennett et al. (2003a). In §6 we establish the Gaussian nature of the *WMAP* anisotropy, determined in the companion paper of Komatsu et al. (2003). In §7 we present the dipole and quadrupole moments and summarize analyses of the angular power spectrum (Hinshaw et al. 2003b; Verde et al. 2003). In §8 we highlight the *WMAP* polarization results, including a detection of the reionization of the universe (Kogut et al. 2003). In §9 we summarize some of the cosmological implications of the *WMAP* results (Page et al. 2003c; Spergel et al. 2003; Peiris et al. 2003). Finally, in §10 we discuss the availability of the *WMAP* data products.

2. OBSERVATIONS

The 840 kg *WMAP* Observatory was launched aboard a Delta II 7425-10 rocket (Delta launch number 286) on 30 June 2001 at 3:46:46.183 EDT from Cape Canaveral. *WMAP* executed three phasing loops in the Earth-Moon system before a lunar-gravity-assist swing-by, a month after launch, catapulted *WMAP* to an orbit about the second Lagrange point of the Sun-Earth system, L_2. Station-keeping is performed approximately four times per year to maintain the Observatory in a Lissajous orbit about the L_2 point with the Earth-*WMAP* vector within about $\sim 1^\circ - 10^\circ$ of the Sun-Earth vector. The phasing loop maneuvers and station-keeping are executed using the *WMAP* propulsion system of blow-down hydrazine and eight thrusters.

The central design philosophy of the *WMAP* mission was to minimize sources of systematic measurement errors (Bennett et al. 2003a). The *COBE* mission proved the effectiveness of a differential design in minimizing systematic errors. Therefore, the *WMAP* instrument was designed with a back-to-back optical system with 1.4 m $\times$ 1.6 m primary reflectors to provide for differential measurements of the sky. The primary and secondary reflectors direct radiation into two focal planes, with ten feed horns in each, as described by Page et al. (2003c).

The beams have a gain pattern, G, which is neither symmetric nor Gaussian. We define the beam solid angle as $\int G(\Omega)/G_{\max}\, d\Omega$. The beam size can be expressed as the square root of the beam solid angles, giving 0.22°, 0.35°, 0.51°, 0.66°, and 0.88° for W-band though K-band, respectively. Alternately, the beams can be expressed in terms of a full-width at half-maximum (FWHM) for each band, given in Table 1. Detailed analyses of the *WMAP* beams are discussed by Page et al. (2003a,c).

The feed horns are attached to orthomode transducers (OMTs) that split the polarization of the incoming signal

Table 1. Approximate Observational Properties by Band

Item	K-Band	Ka-Band	Q-Band	V-Band	W-Band
Wavelength, λ (mm)	13	9.1	7.3	4.9	3.2
Frequency, ν (GHz)	22.8	33.0	40.7	60.8	93.5
Ant./therm. conversion factor, $\Delta T/\Delta T_A$	1.014	1.029	1.044	1.100	1.251
Noise, σ_0 (mK) $\sigma = \sigma_0 N_{obs}^{-1/2}$	1.424	1.449	2.211	3.112	6.498
Beam width θ(°FWHM)	0.82	0.62	0.49	0.33	0.21
No. of Differencing Assemblies	1	1	2	2	4
No. of Radiometers	2	2	4	4	8
No. of Channels	4	4	8	8	16

into a differential correlation radiometer system with High Electron Mobility Transistor (HEMT) amplifiers. There are ten "differencing assemblies" each consisting of two "radiometers" with two "channels" each (Jarosik et al. 2003a; Bennett et al. 2003a). There are four W-band ($\sim$ 94 GHz), two V-band ($\sim$61 GHz), two Q-band ($\sim$ 41 GHz), one Ka-band ($\sim$ 33 GHz), and one K-band ($\sim$ 23 GHz) differencing assemblies. We usually refer to these bands by the generic designations K, Ka, Q, V, and W because there are multiple radiometers in each band, whose precise frequencies are not identical. Also, the effective frequency of a radiometer depends on the spectrum of the emission it detects. Precise frequencies for the radiometers for a CMB anisotropy spectrum are given by Jarosik et al. (2003a). Polynomials are given to determine the effective frequency of the radiometers depending on the emission frequency spectrum. See Table 1 for a summary of radiometer properties.

Undesirable $1/f$ noise is minimized by the design of the *WMAP* radiometers (Jarosik et al. 2003a). All radiometers have $1/f$ knees below 50 mHz; 18 of 20 are below 10 mHz; and 10 of the 20 are below 1 mHz Jarosik et al. (2003b). (The $1/f$ knee is defined as the frequency where the noise power spectral density is $\sqrt{2}$ times higher than its high frequency value.) Jarosik et al. (2003a) demonstrate that all radiometer outputs have Gaussian noise, which "integrates down" with time as expected.

The radiometers are passively cooled to $\sim$ 90 K with no mechanical refrigerators. In addition, no actively cycling heaters were permitted anywhere on the *WMAP* spacecraft. These design features helped to ensure a mechanically, thermally, and electronically quiet platform that minimizes the driving forces of systematic measurement errors.

In addition to the differential design, the *COBE* mission also demonstrated the importance of scanning large areas of the sky in a short period of time with a complex scan pattern. *WMAP* follows the *COBE* example with a three-axis (three reaction wheel) control system that maintains the Observatory in a nearly constant survey mode of operations. (The Observatory is in constant survey mode, except for only $\sim$ 1 hr for each of $\sim$ 4 station-keeping maneuvers per year.) In survey mode, the optical boresight sweeps out a complex pattern on the sky (Bennett et al. 2003a). Approximately 30% of the sky is observed each hour. The Observatory spins at 0.464 rpm ($\sim$7.57 mHz) and precesses at 1 rev hr^{-1} ($\sim$ 0.3 mHz).

Six months are required for L_2 to orbit half way around the Sun, allowing for full sky coverage. The observations presented in this and companion papers include a full orbit about the Sun, thus containing two sets of full sky observations. By 10 August 2001, *WMAP* was sufficiently stable in its L_2 orbit for CMB data-taking to commence. One year of observations, completed on 9 August 2002, were analyzed. Data taken beyond this date will be the subject of future analyses.

3. DATA PROCESSING, CALIBRATION, & SYSTEMATIC ERRORS

Time-ordered telemetry data from the Observatory are down-linked via NASA's Deep Space Network (DSN) to the *WMAP* Science and Mission Operations Center (SMOC) at the Goddard Space Flight Center. The data are then transferred to the *WMAP* Science Team for analysis. All of the instrument data are down-linked to the ground without any on-board flight data processing, thus allowing full insight into potential systematic effects.

Only a fraction of a percent of data was lost in the flow from the Observatory to the SMOC. About 1% of the received data were not used due to systematic error concerns (e.g., data taken during near station-keeping maneuvers). Of the $\sim$ 99% good data, the processing pipeline flagged observations where bright planets were in the beams so that these data would not used be used in making maps. The statistics on lost, bad, and flagged data are given in Table 2.

An overview of the data flow is shown in Figure 1. The heart of the data analysis efforts center on studies of systematic measurement errors (Hinshaw et al. 2003b). Components of spurious signals at the spin period are

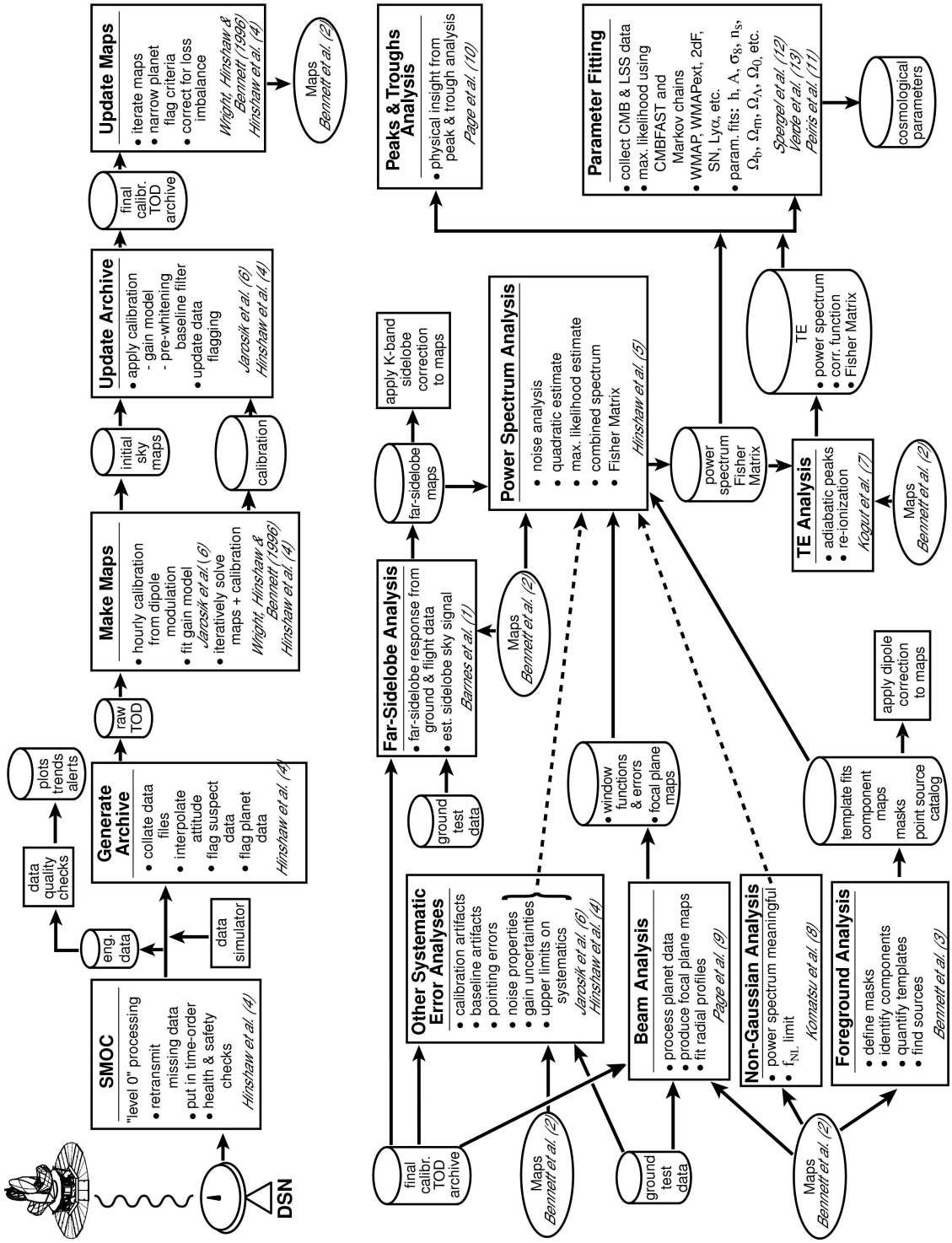

Fig. 1.— An overview of the *WMAP* data flow. The references are: (1) Barnes et al. (2003) (2) Bennett et al. (2003b) (3) Bennett et al. (2003c) (4) Hinshaw et al. (2003b) (5) Hinshaw et al. (2003a) (6) Jarosik et al. (2003b) (7) Kogut et al. (2003) (8) Komatsu et al. (2003) (9) Page et al. (2003a) (10) Page et al. (2003b) (11) Peiris et al. (2003) (12) Verde et al. (2003).

the most difficult to distinguish from true sky signals. The Observatory was designed to minimize all thermal and voltage variations and all susceptibilities to these variations, especially at the spin period, as discussed in §2 and by Bennett et al. (2003a). In addition, high precision temperature monitors on the Observatory provide the data needed to verify that systematic errors from thermal variations are negligible. Jarosik et al. (2003b) report that in-flight spin-synchronous effects from the radiometers are $< 0.17\ \mu$K rms in the time-ordered-data (TOD), based on flight thermal variations multiplied by upper limits on component susceptibilities measured in ground testing. Analysis of flight data without use of characterizations derived from ground-based testing give $< 0.14\ \mu$K rms from all sources (not just the radiometers). This is a factor of > 50 times smaller than the requirement that was set in the mission's systematic error budget. Thus, *no corrections to the first year WMAP data are required for spin-synchronous systematic errors.*

The core of the processing pipeline calibrates the data and converts the differential temperatures into maps. The data are calibrated based on the Earth-velocity modulation of the CMB dipole. A gain model of the radiometers was derived and fit by Jarosik et al. (2003b). The model is based on the constancy of the dipole signal on the sky, the measured physical temperature of the front-end radiometer components, and on the time-averaged RF-bias (total power) of the radiometer outputs. This relatively simple model closely matches the gains derived from the hourly measurements of the amplitude of the dipole and is used in *WMAP* data processing. Calibration is achieved within 0.5% accuracy, dominated by the statistical uncertainty in the absolute calibration.

Low levels of $1/f$ noise create stripes in the maps that affect the angular power spectrum and other statistics derived from the maps. A pre-whitening filter is applied to the TOD to minimize these artifacts. An estimate of the magnitude of the striping is given in Hinshaw et al. (2003b) for the maps, and by Hinshaw et al. (2003a) for the power spectrum.

The differential temperature data are formed into maps based on the technique introduced by Wright et al. (1996b). HEALPix[11] is used to define map pixels on the sky in Galactic coordinates. Various levels of resolution are specified by a "resolution level" with an integer ($r = 0, 1, 2, \ldots$). With $N_{\rm side} = 2^r$, the number of pixels in the map is $N_{\rm pix} = 12\ N_{\rm side}^2$. The area per pixel is $\Omega_{\rm pix} = 4\pi/N_{\rm pix}$ and the separation between pixel centers is $\theta_{\rm pix} = \Omega_{\rm pix}^{1/2}$. For example, HEALPix resolution level $r = 9$ (used in *WMAP* map-making) corresponds with $N_{\rm side} = 512$, $N_{\rm pix} = 3\,145\,728$, $\Omega_{\rm pix} = 3.99 \times 10^{-6}$ sr, and $\theta_{\rm pix} = 0\overset{\circ}{.}115 = 6.87$ arc-min.

WMAP observes the sky convolved with the beam pattern. This is equivalent to the the spatial transform of the sky multiplied by the instrument's "window function." The beam patterns are measured in-flight from observations of Jupiter (Page et al. 2003a). Uncertainties in our knowledge of the beam pattern, although small, are a significant source of uncertainty for *WMAP* since they imply imperfect knowledge of the window function. A small difference between the A-side and B-side optical losses was derived based on dipole observations and corrected in the processing. Far sidelobes of the beam patterns, determined by ground measurements and in-flight using the Moon, have been carefully examined (Barnes et al. 2003). A small far-sidelobe correction is applied only to the K-band map. We now describe the maps.

4. THE MAPS

We combine the radiometer results within each band and present the five full sky maps at effective CMB anisotropy frequencies 23, 33, 41, 61, and 94 GHz in Figures 2a, 2b, 2c, 2d, 2e. The maps are shown in the Mollweide projection in units of CMB thermodynamic temperature. The number of independent observations that contribute to

[11] http://www.eso.org/science/healpix/

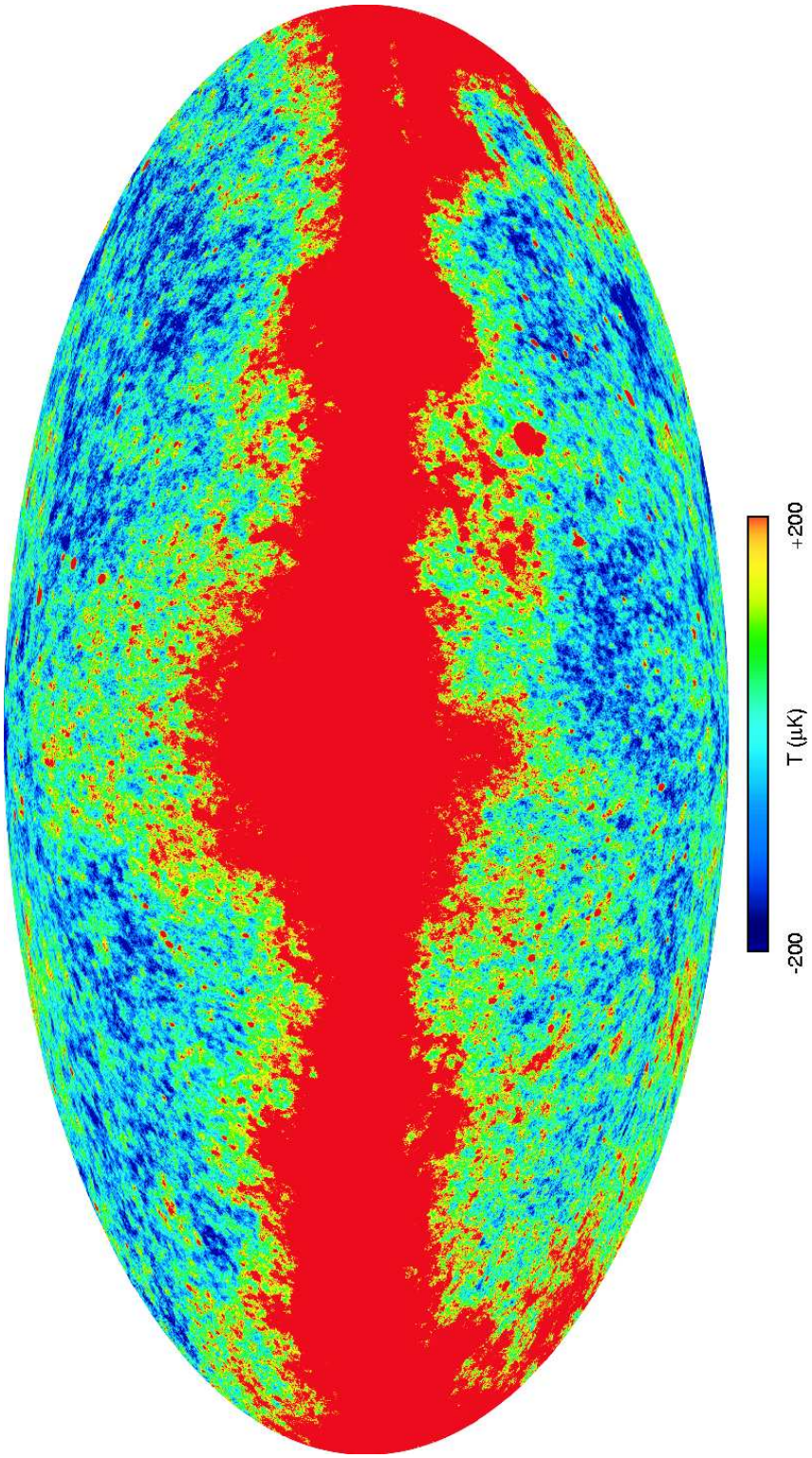

Fig. 2a.— The K-band full sky map in Galactic coordinates, shown in a Mollweide projection.

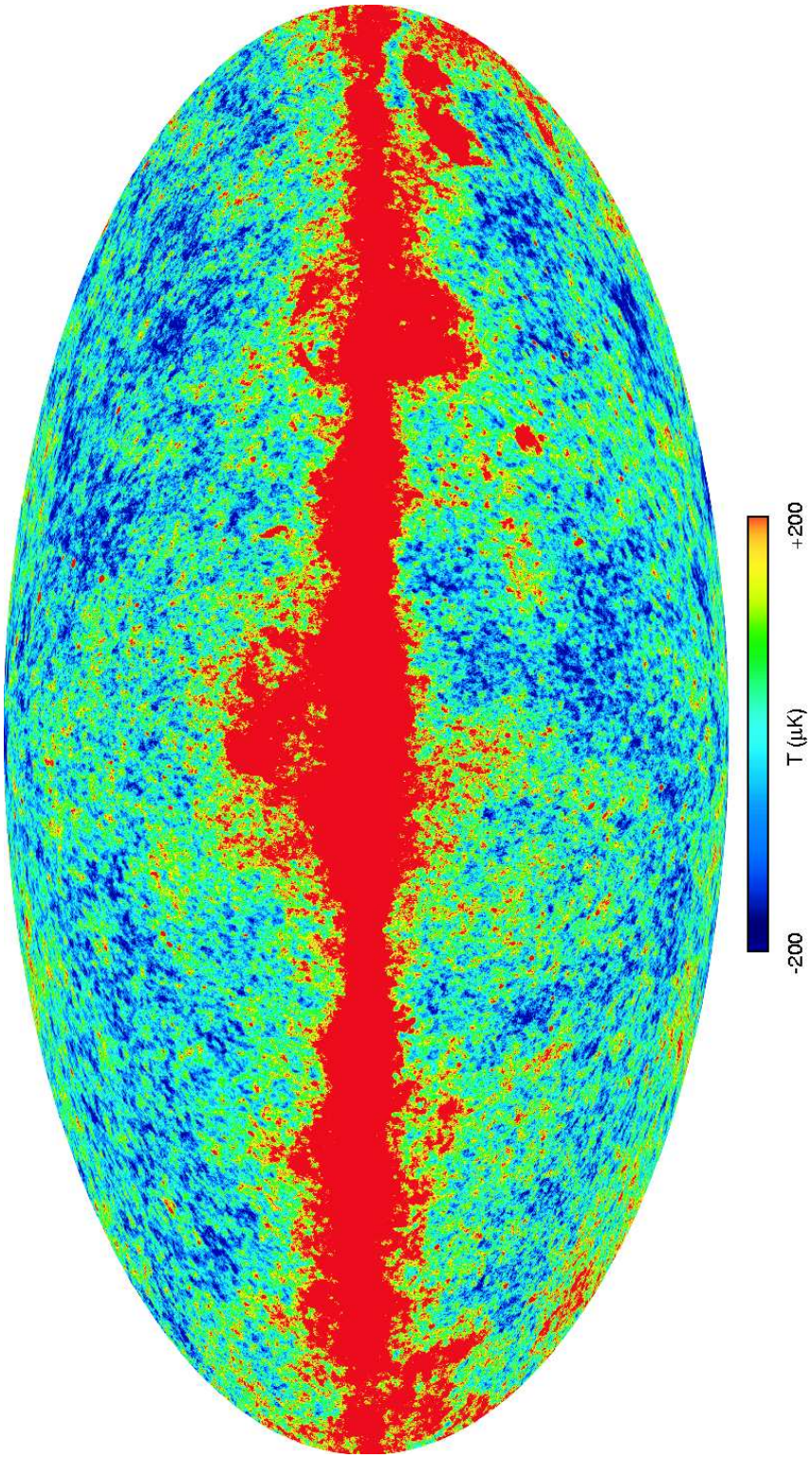

Fig. 2b.— Ka-band

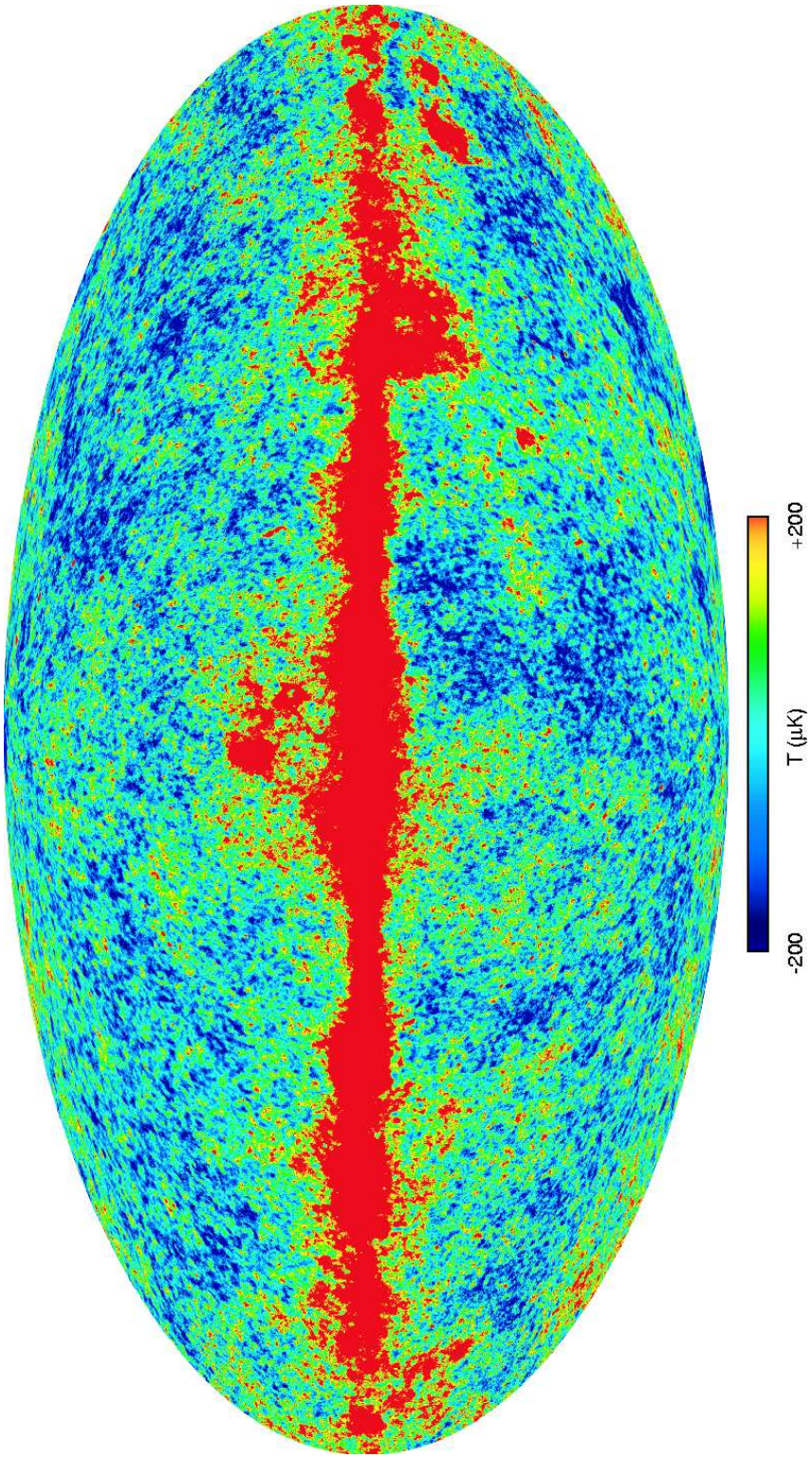

Fig. 2c.— Q-band

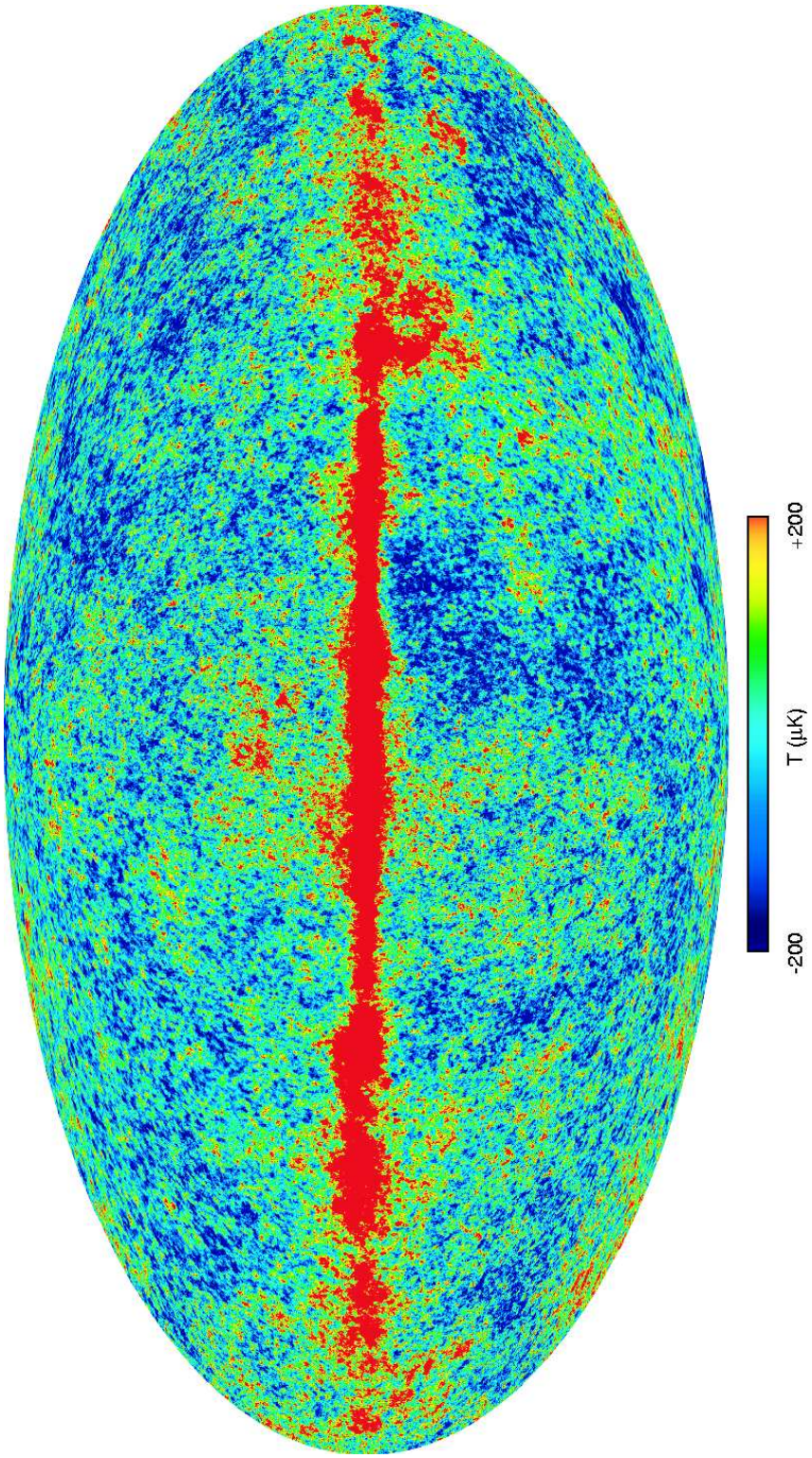

Fig. 2d.— V-band

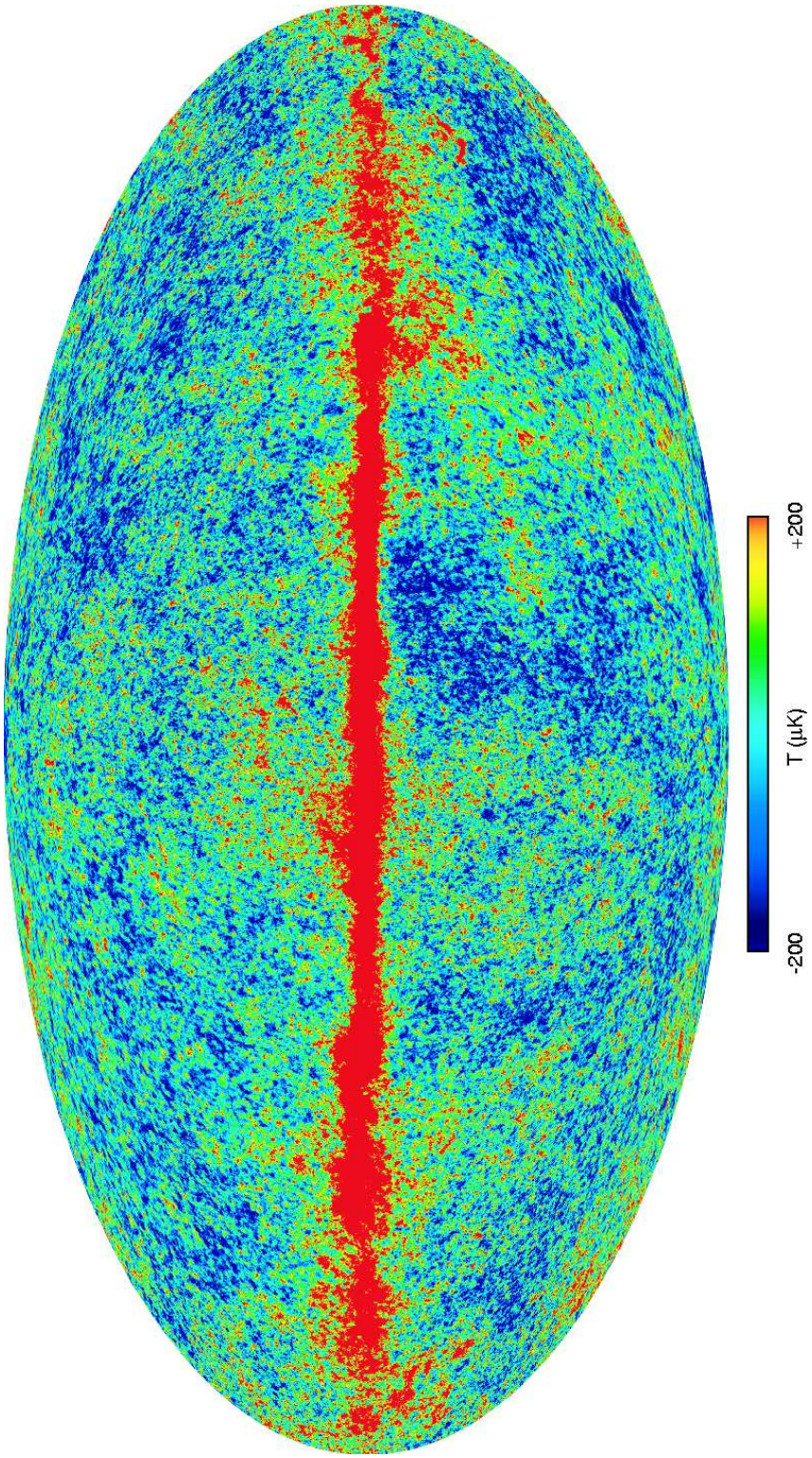

Fig. 2e.— W-band

each pixel form the sky pattern in Figure 3. Figure 4 provides an overall guide to some of the more prominent features of the maps as well as point sources detected by *WMAP*, as described by Bennett et al. (2003b).

Figure 5 shows the K-band and Ka-band maps, with the Ka-band map smoothed to K-band resolution. Note both the significant decrease in Galactic signal from K-band to Ka-band and the high Galactic latitude similarities of the CMB between the maps. Likewise, Figure 6 shows the Q-band, V-band, and W-band maps with the latter two smoothed to Q-band resolution. Higher Galactic contamination in Q-band is apparent. Both Figures 5 and 6 highlight the consistency of the high Galactic latitude CMB anisotropy pattern from band to band.

Comparisons of data between *WMAP* radiometers, and between *WMAP* and *COBE*, are important indicators of systematic error levels. Figure 7 illustrates the enormous improvement in angular resolution from *COBE* to *WMAP*. Features in the maps appear to be generally consistent, but the consistency is better addressed by a more direct comparison. To do this we take a combination of the *WMAP* Q-band and V-band maps and smooth it to mimic a *COBE*-DMR 53 GHz map (see Figure 8). We then examine the difference between the *COBE* and *WMAP* pseudo-map. Figure 9 shows the difference map along with a simulated map of the noise. With the exception of a feature in the Galactic plane, the agreement is clearly at the noise level. The Galactic plane feature is likely to be a result of the spectral index uncertainty of combining the Q-band and V-band maps to make a 53 GHz equivalent map.

5. FOREGROUND ANALYSES

An understanding of diffuse Galactic emission and extragalactic point sources is necessary for CMB analyses. The *WMAP* mission carries radiometers at five frequencies for the purpose of separating the CMB anisotropy from foreground emission based on their different spectra. Figure 10 illustrates the spectral difference between the CMB and foregrounds. The *WMAP* bands were selected to be near the frequency where the ratio of the CMB anisotropy to the contaminating foreground is at a maximum.

5.1. Masks

For CMB analyses it is necessary to mask out regions of bright foreground emission. Bennett et al. (2003c) present a recipe for foreground masks based on K-band temperature levels. Since foreground contamination is most severe in K-band, it is used as the best tracer of contamination. The contamination morphology is similar enough across all five *WMAP* bands that masks based on the temperature levels in other bands would be redundant and unnecessary. Standard names are given for the mask levels. For example, the Kp0 mask cuts 21.4% of sky pixels while the Kp2 mask cuts 13.1%. See Bennett et al. (2003c) for further detail. An extragalactic point source mask is also constructed based on selections from source catalogs. An additional 2% of pixels are masked due to these ~ 700 sources.

5.2. Diffuse Galactic emission

Beyond the use of masks, one technique for reducing the level of foreground contamination is to form a linear combination of the multifrequency *WMAP* data that retains unity response for only the emission component with a CMB spectrum. This technique was introduced for *COBE* by Bennett et al. (1992). With five *WMAP* bands instead of the three on *COBE*, and with a somewhat more elaborate approach for *WMAP*, Bennett et al. (2003c) arrive at the internal (*WMAP* data only) linear combination map seen in Figure 11 of this paper. The foregrounds are removed to

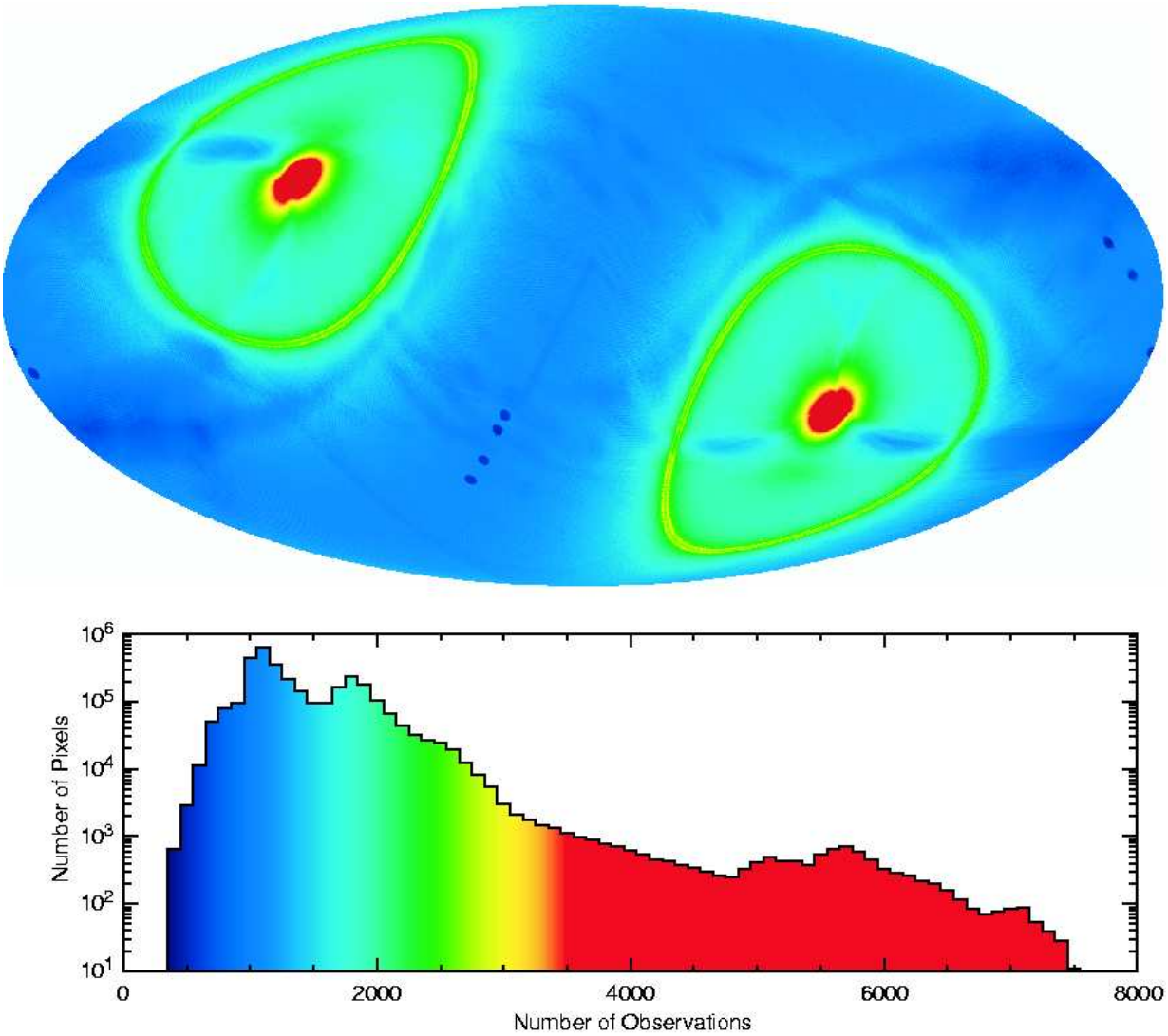

Fig. 3.— The number of independent observations per pixel in Galactic coordinates. The number of observations is greatest at the ecliptic poles and in rings around the ecliptic poles with diameters corresponding to the separation angle of the two optical boresight directions (approximately 141°). The observations are the most sparse in the ecliptic plane. Small area cuts are apparent where Mars, Saturn, Jupiter, Uranus, and Neptune data are masked so as not to contaminate CMB analyses. Jupiter data are used for beam mapping. The histogram of the sky sampling shows the departures from uniform sky coverage.

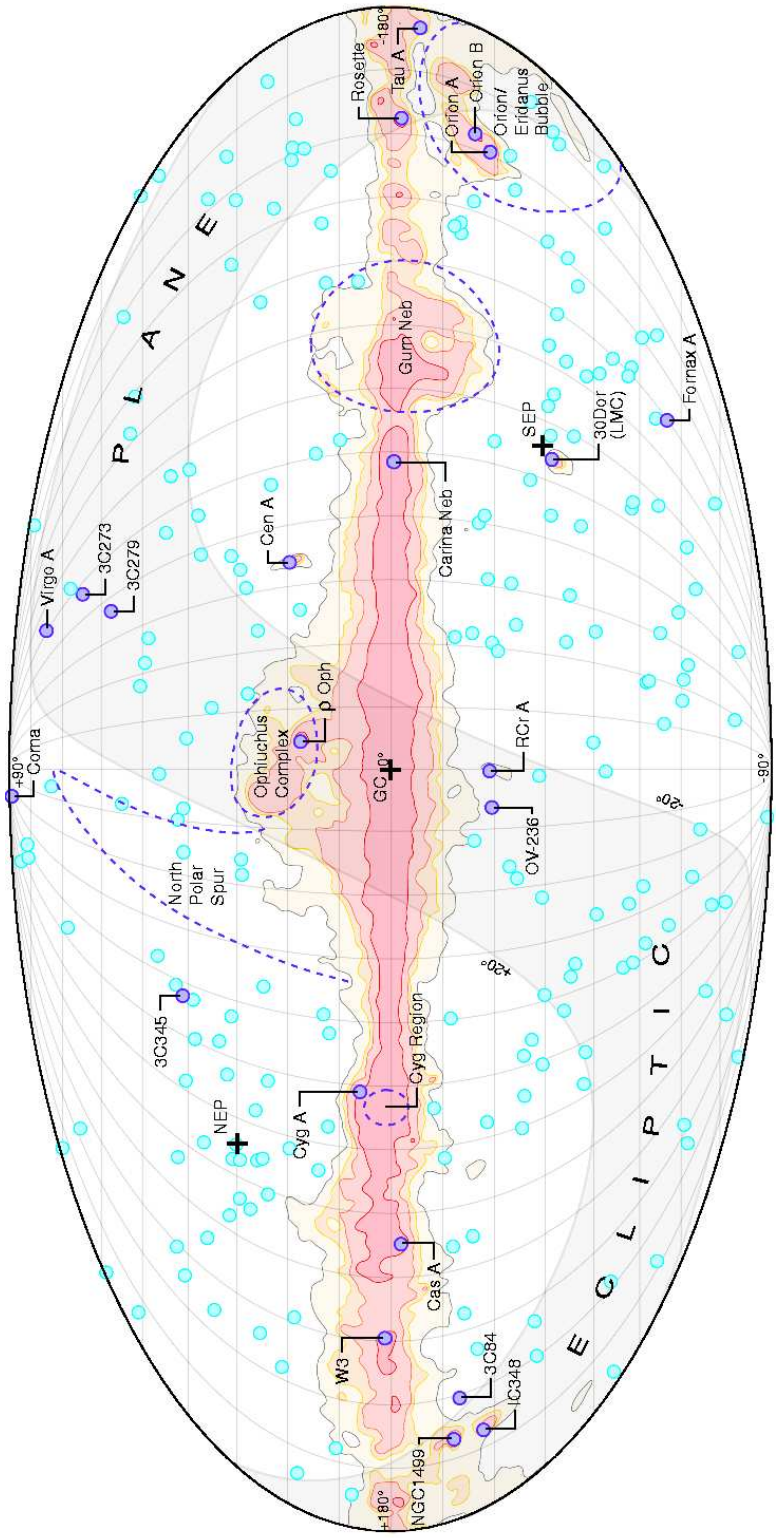

Fig. 4.— A guide to the microwave sky for reference. This picture shows the large-scale emission from the Milky Way galaxy, including some of its notable components such as the Cygnus complex, the North Polar Spur, the Gum region, etc. The small circles show positions of the microwave point sources detected by *WMAP* (Bennett et al. 2003c). The brighter sources are labeled for reference.

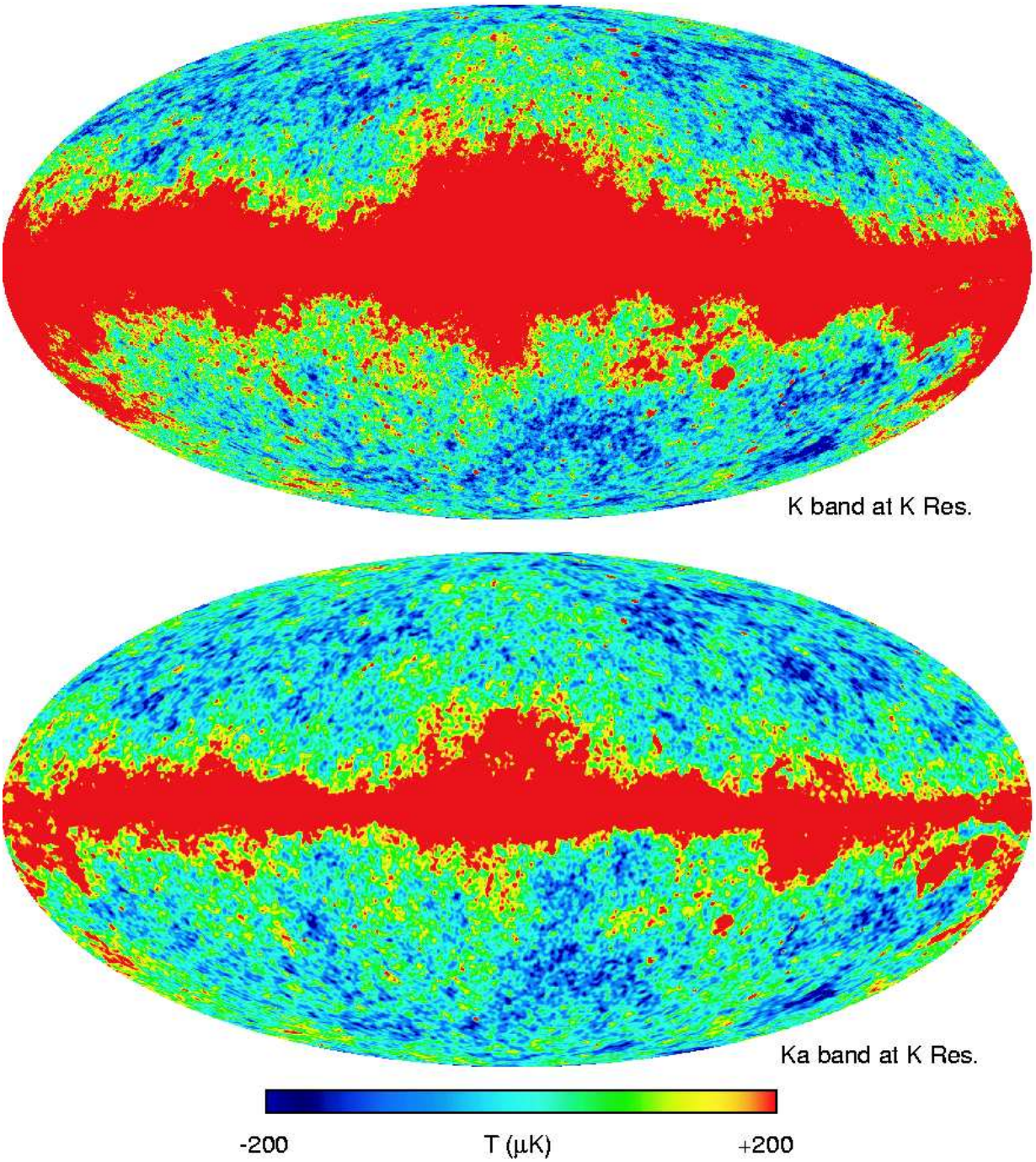

Fig. 5.— A comparison of the K-band map with the Ka-band map smoothed to K-band resolution, both in thermodynamic temperature, shows the dramatic reduction of Galactic contamination with increased frequency. The comparison also shows the similarity of the CMB fluctuation features at high Galactic latitude.

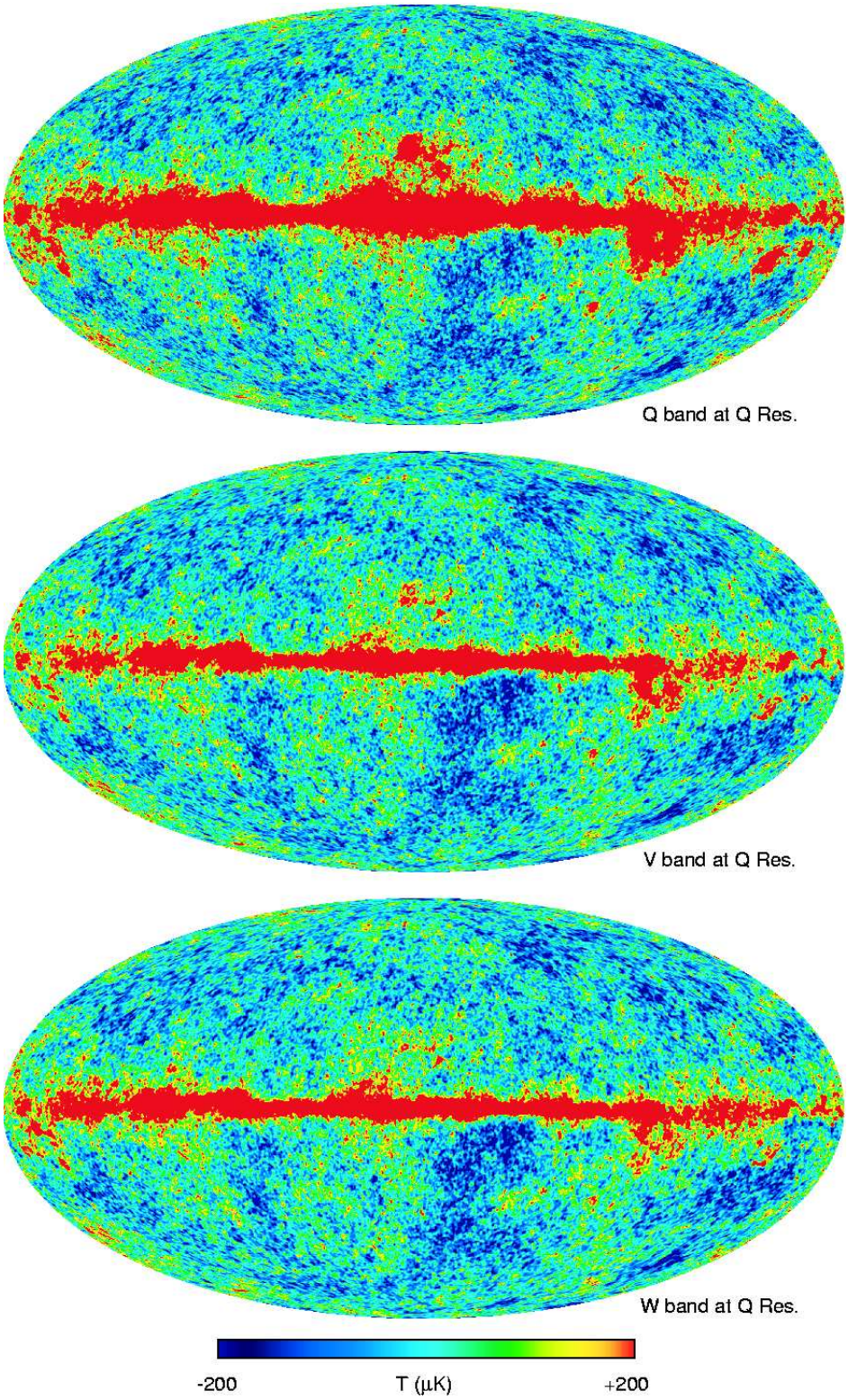

Fig. 6.— A comparison of the Q-band, V-band, and W-band maps. All three maps are smoothed to Q-band resolution and are in thermodynamic temperature. The reduction of Galactic contamination relative to K-band and Ka-band (Figure 5) is apparent. The maps show that the constant features across bands are CMB anisotropy while the thermodynamic temperature of the foregrounds depends on the band (frequency).

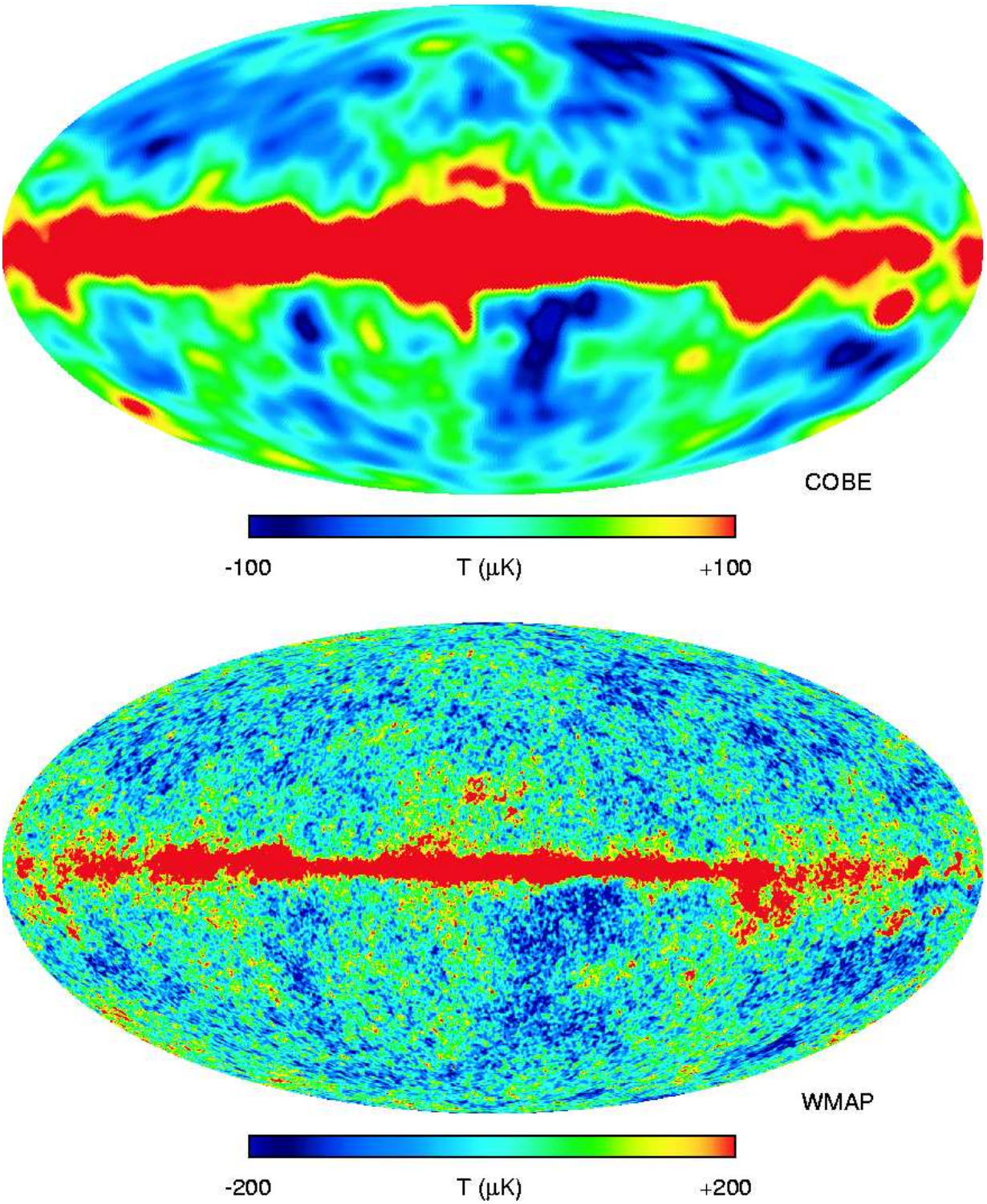

Fig. 7.— A comparison of the *COBE* 90 GHz map (Bennett et al. 1996) with the W-band *WMAP* map. The *WMAP* map has 30 times finer resolution than the *COBE* map.

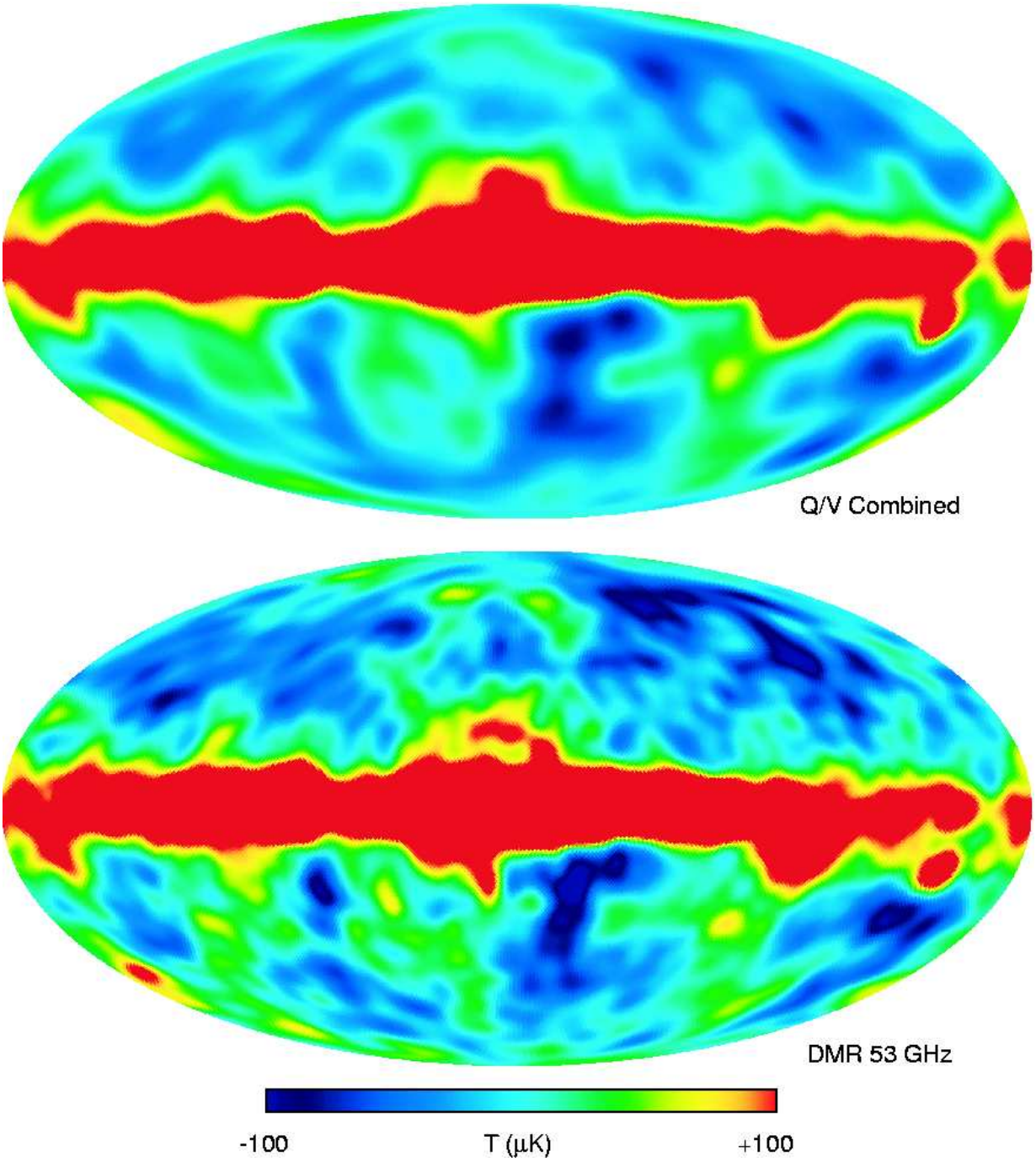

Fig. 8.— The *COBE*-DMR 53 GHz map (Bennett et al. 1996) is shown along with a map made with a linear combination of the Q-band and V-band *WMAP* maps to mimic a 53 GHz map. Note the strong similarity of the maps.

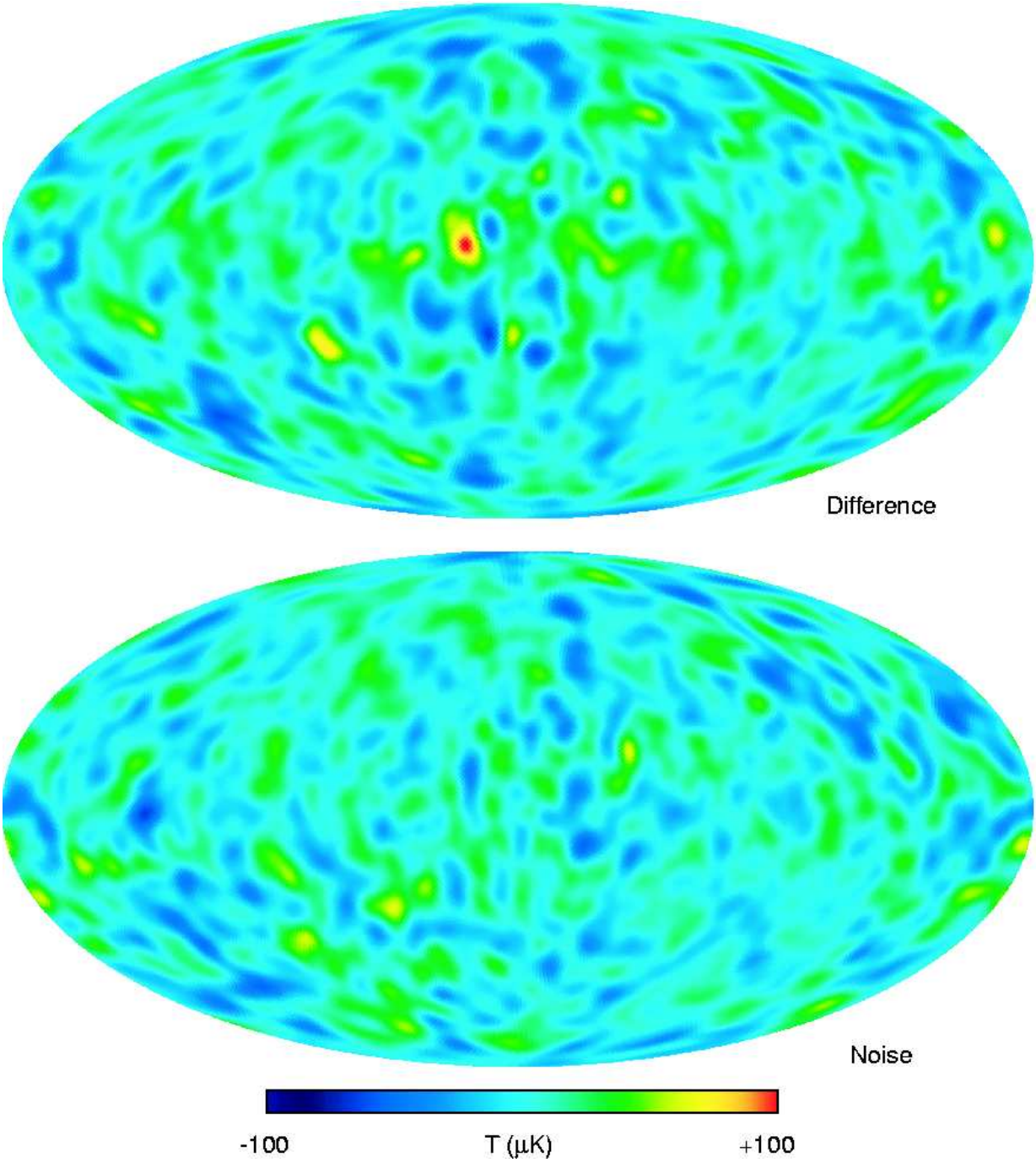

Fig. 9.— The difference map is shown between the *COBE*-DMR 53 GHz map and the combination Q-band/V-band maps from Figure 8. This is compared with a map of the noise level. The maps are consistent with one another with the exception of a feature in the galatic plane. This discrepancy is likely to be due to a spectral index that is sufficiently different from the assumed CMB spectrum used to combine the *WMAP* Q-band and V-band maps to mimic a 53 GHz map.

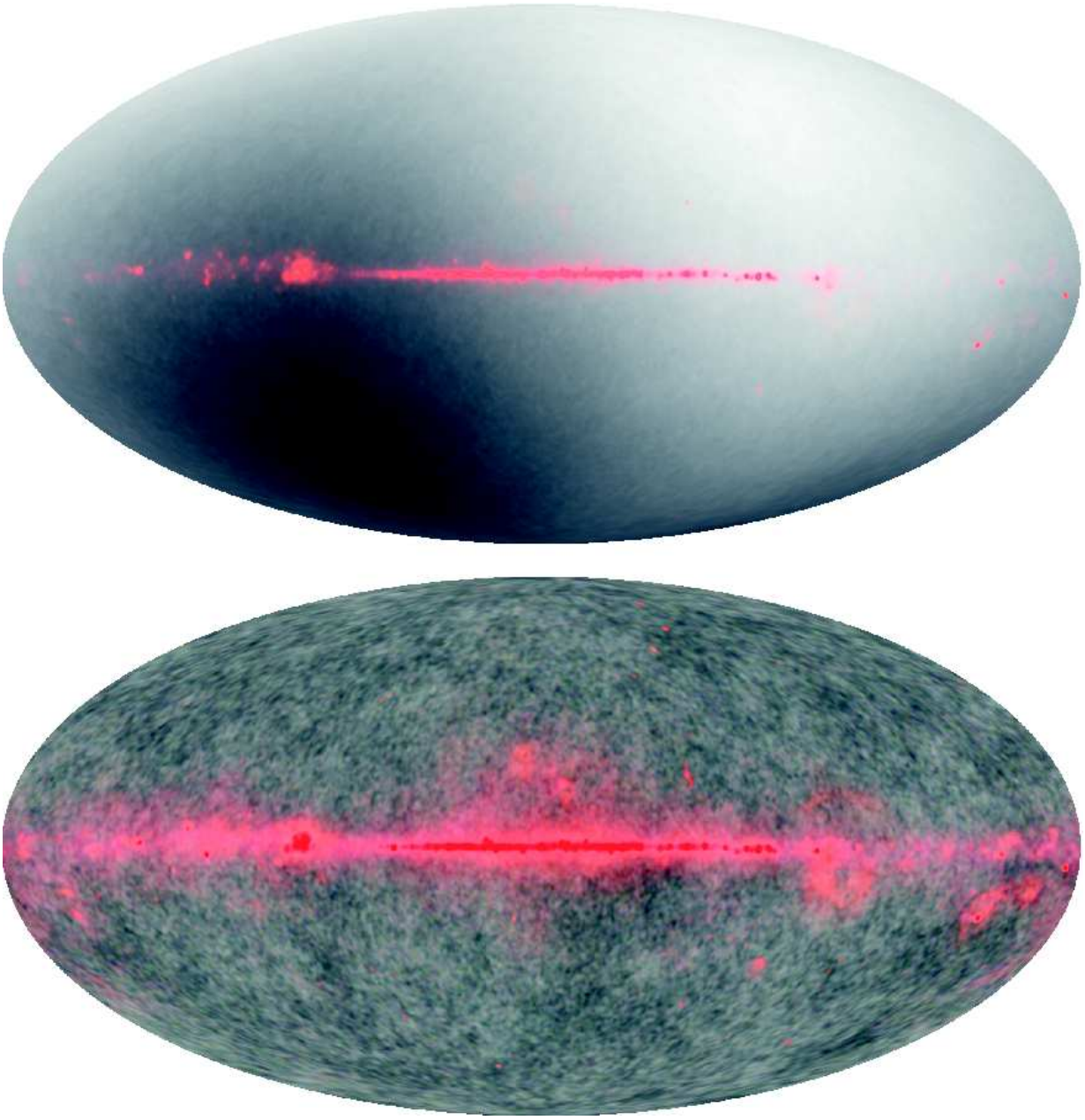

Fig. 10.— False color images represent the spectral information from mutliple *WMAP* bands. Q-band is red, V-band is green, and W-band is blue. A CMB thermodynamic spectrum is grey. (*top*) A three color combination image from the Q-, V-, and W-band maps. The dipole and high Galactic latitude anisotropy are seen. (*bottom*) A similar false color image but with the dipole subtracted.

a remarkable degree; however, the statistics of this internal linear combination map are complex and inappropriate for most CMB analyses.

Below, we use the notation convention that flux density is $S \sim \nu^{\alpha}$ and antenna temperature is $T_A \sim \nu^{\beta}$, where the spectral indices are related by $\beta = \alpha - 2$. In general, the CMB is expressed in terms of thermodynamic temperature, while Galactic and extragalactic foregrounds are expressed in antenna temperature. Thermodynamic temperature differences are given by $\Delta T = \Delta T_A[(e^x - 1)^2/x^2 e^x]$, where $x = h\nu/kT_0$, h is the Planck constant, ν is frequency, k is the Boltzmann constant, and $T_0 = 2.725$ K is the CMB temperature (Mather et al. 1999). Values of $\Delta T/\Delta T_A$ for the *WMAP* bands are given by Jarosik et al. (2003b) and can be found in Table 1.

Bennett et al. (2003c) identify the amplitudes and spectral indices of the individual emission components. A maximum entropy method (MEM) approach is adopted where priors are used for component amplitudes and spectral indices, except for free-free emission, which has a fixed spectral index (–2.15 in the *WMAP* bands). An iterative fit is performed, where the pixel-by-pixel amplitudes are updated in accordance with the MEM residuals until low ($< 1\%$) residuals are achieved. The process results in a map of each emission component for each of the five *WMAP* bands. The derived maps of thermal emission from dust give a uniform spectral index across the sky of $\beta_d \approx 2.2$. The derived map of free-free emission is reasonable given the amplitude and morphology of Hα measurements. The other radio component fit should include the combined emission of synchrotron and spinning dust. It shows the synchrotron spectrum steepening with increasing frequency, as would be expected for a spectral break due to synchrotron losses at ≈ 20 GHz. There is no indication of the less steep or flattening spectral index that would result from spinning dust emission. Thus spinning dust emission is limited to $< 5\%$ of the total Ka-band foreground. Reports of dust-correlated microwave emission from *COBE* data analyses are understood as an admixture of the fraction of synchrotron emission (with $\beta \approx -3$) that is traced by a dust template, and thermal dust emission ($\beta \approx 2.2$), giving a combined spectral index of $\beta \approx -2.2$ between the *WMAP* Ka-band and V-band, approximating the *COBE* 31 GHz and 53 GHz bands.

While the MEM method is useful for understanding the nature of the foreground emission components, these results can not be directly used in CMB analyses due to the complex noise properties that result from the MEM process and its simultaneous use of multifrequency maps. For the CMB analyses we use a mask (usually Kp2) to exclude pixels where the Galactic emission is strong, combined with template fitting (using external data only) where the foregrounds can be adequately corrected. This approach does not complicate the noise properties of the maps. Bennett et al. (2003c) describe the template fitting in detail. Thermal dust emission has been mapped over the full sky in several infrared bands, most notably by the *COBE* and *IRAS* missions. A full sky template is provided by Schlegel et al. (1998), and is extrapolated in frequency by Finkbeiner et al. (1999). The mostly synchrotron emission map of Haslam et al. (1981) at 408 MHz is used as a radio template. The free-free ionized gas is traced by the Hα map assembled by Finkbeiner (2003) from the Wisconsin H-Alpha Mapper (WHAM), the Virginia Tech Spectral-Line Survey (VTSS), and the Southern H-Alpha Sky Survey Atlas (SHASSA) (Dennison et al. 1998; Haffner et al. 2002; Reynolds et al. 2002; Gaustad et al. 2001) . The foreground contamination remaining after subtraction of the template-fit component is $< 7\ \mu$K rms at Q-band and $< 3\ \mu$K rms at both V-band and at W-band for $l < 15$.

5.3. Point sources

A search was made for point sources in the *WMAP* data. A catalog of 208 detected sources (with 98% reliability) is provided by Bennett et al. (2003c). The derived source counts give a power spectrum level of $C^{\rm src} = (15 \pm 3) \times 10^{-3}\ \mu{\rm K}^2{\rm sr}$ at Q-band. This is consistent with the level found in the bispectrum analysis of the maps (Komatsu et al. 2003) and the level found in fits to the map power spectra (Hinshaw et al. 2003b). We have confidence that the point source level is understood since it is independently derived using three different methods.

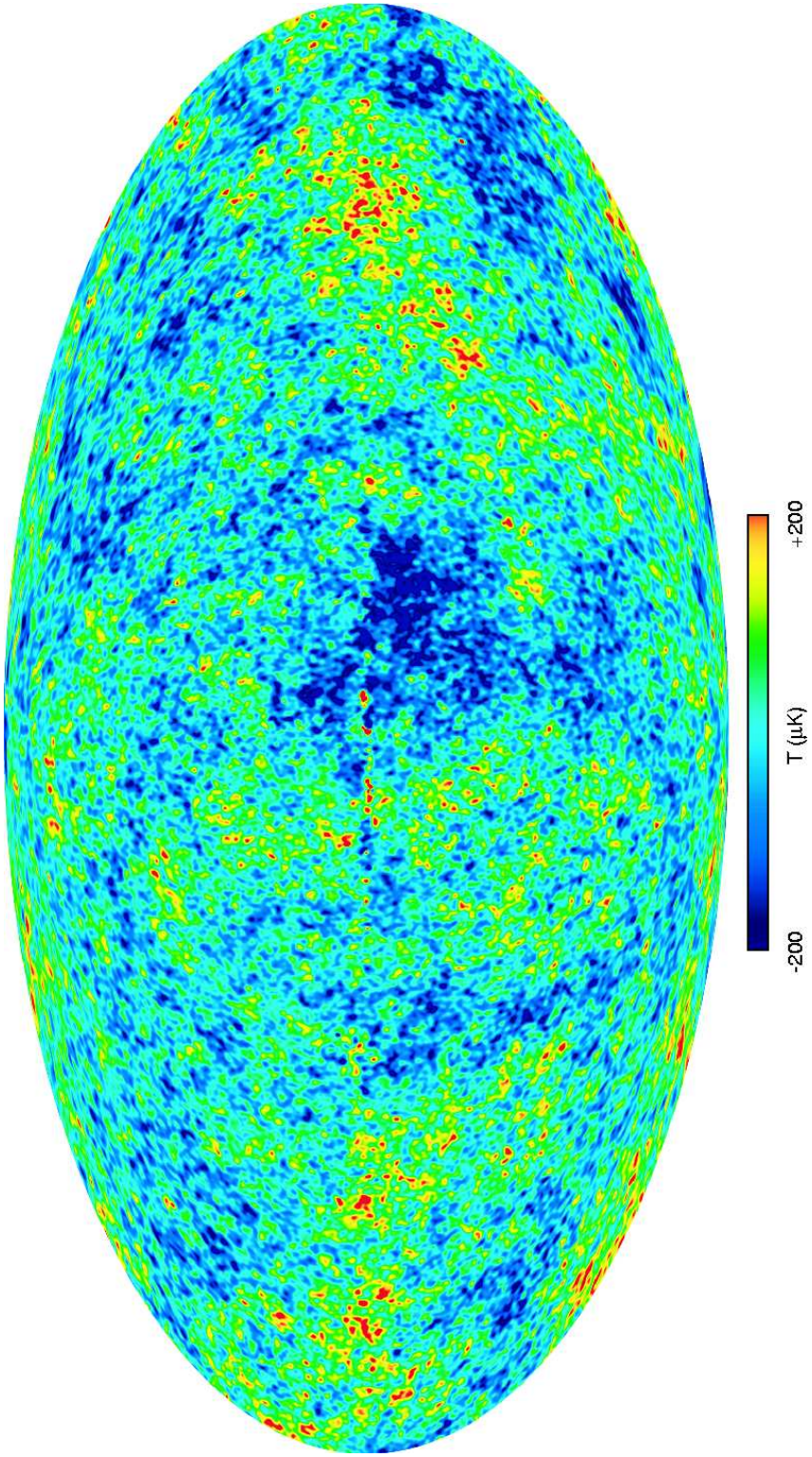

Fig. 11.— This "internal linear combination" map combines the five band maps in such as way as to maintain unity response to the CMB while minimizing foreground foreground contamination. For a more detailed description see Bennett et al. (2003c). For the region that covers the full sky outside of the inner Galactic plane, the weights are $0.109, -0.684, -0.096, 1.921, -0.250$ for K, Ka, Q, V, and W bands, respectively. Note that there is a chance alignment of a particularly warm feature and a cool feature near the Galactic plane. As discussed in Bennett et al. (2003c), the noise properties of this map are complex, so it should not generally be used for cosmological analyses.

5.4. Sunyaev-Zeldovich (SZ) effect

Hot gas in clusters of galaxies imparts energy to the CMB photons, causing a temperature decrement in the *WMAP* bands (the Sunyaev-Zeldovich Effect). The Coma cluster is expected to have the most pronounced signature. For the highest resolution maps, Bennett et al. (2003c) get -0.34 ± 0.18 mK in W-band and -0.24 ± 0.18 mK in V-band in the direction of Coma. Use of the XBACS catalog of X-ray clusters as a template results in -0.36 ± 0.14. This verifies that the Sunyaev-Zeldovich Effect is barely detectable in even a matched search of the *WMAP* sky maps and therefore it is not a significant "contaminant" to the *WMAP* data.

6. LIMITS ON NON-GAUSSIANITY

Maps of the sky are the most complete and compact representation of the CMB anisotropy. Cosmological analyses are based on statistical properties of the maps with the power spectrum as one of the most commonly derived statistics. The power spectrum is a complete representation of the data only if the CMB anisotropy is Gaussian. Also, the most common cosmological models predict that the CMB anisotropy should be consistent with a Gaussian random field (at least at levels that are currently possible to measure). Therefore, we test the Gaussianity of the anisotropy, both to interpret the power spectrum (and other statistical derivatives of the maps) and to test cosmological paradigms.

There is no single best test for Gaussianity. Specific tests can be more or less sensitive to different assumed forms of non-Gaussianity. Komatsu et al. (2003), in a companion paper, search for non-Gaussianity in the *WMAP* CMB anisotropy maps using Minkowski functionals and a bispectrum estimator.

Minkowski functionals (Minkowski 1903; Gott et al. 1990) quantify topological aspects of the CMB maps. Anisotropy is examined via contours at different temperature levels, and the number and areas of regions enclosed by these contours are computed. Three Minkowski functionals are the area represented by hot and cold spots, the contour length around these areas, and the difference between the number of these areas (the "genus").

It is widely believed that the CMB anisotropy arises from Gaussian linear fluctuations in the gravitational potential. Komatsu & Spergel (2001) suggest that non-Gaussian anisotropy be considered as the next, quadratic, term of a curvature perturbation Taylor expansion. The coefficient of the quadratic (mean-square) non-Gaussian term is a non-linear coupling parameter, f_{NL}. Since the CMB bispectrum measures the phase correlations of the anisotropy, it can be used to solve for f_{NL}. The Minkowski functional results can also be expressed in terms of f_{NL}.

For the Minkowski functionals, Komatsu et al. (2003) find $f_{NL} < 139$ (95% CL). From the bispectrum, Komatsu et al. (2003) find $-58 < f_{NL} < 134$ (95% CL). The two results are consistent. The CMB anisotropy is thus demonstrated to follow Gaussian statistics. This is a significant result for models of the early universe. It also means that we can construct and interpret CMB statistics (e.g. the angular power spectrum) from the maps in a straightforward manner.

7. MULTIPOLES

The temperature anisotropy, $T(\mathbf{n})$, is naturally expanded in a spherical harmonic basis, Y_{lm}, as

$$T(\mathbf{n}) = \sum_{l,m} a_{lm} Y_{lm}(\mathbf{n}). \tag{1}$$

The angular power spectrum, C_l, is a cosmological ensemble average given by

$$C_l = \langle |a_{lm}|^2 \rangle \tag{2}$$

and is observed for our actual sky as

$$C_l^{sky} = \frac{1}{2l+1}\sum_m |a_{lm}|^2. \tag{3}$$

Assuming random phases, the temperature anisotropy for each multipole moment, ΔT_l, can be associated with the angular spectrum, C_l, as

$$\Delta T_l = \sqrt{C_l^{sky}\, l(l+1)/2\pi}. \tag{4}$$

The correlation function is

$$C(\theta) = \frac{1}{4\pi}\sum_l \sum_{m=-l}^{+l} C_l P_l(cos\,\theta) \tag{5}$$

$$= \frac{1}{4\pi}\sum_l (2l+1) C_l\, P_l(cos\,\theta) \tag{6}$$

where P_l is the Legendre polynomial or order l.

In practice, an instrument adds noise and spatially filters the sky signal due to the beam pattern and any other experimental limitations on the sampling of all angular scales. The experimental transfer function, b_l, for each multipole moment depends upon the specific beam pattern of the experiment. *WMAP* samples all angular scales limited only by the beam pattern. The window function for the signal power between channels i and j is

$$w_l^{ij} = b_l^i b_l^j p_l^2, \tag{7}$$

where p_l^2 is the pixel window function. The angular power spectrum then becomes

$$C_l = C_l^{ij} b_l^i b_l^j + N_l^i \delta_{ij} \tag{8}$$

where N_l^i is the power spectrum noise that results from the instrument noise, which is assumed to be uncorrelated between channels i and j.

The use of a sky mask for foreground suppression breaks the orthogonality of the spherical harmonics on the sky and leads to mode coupling. Hinshaw et al. (2003b) discuss how *WMAP* handles this, and other complexities.

7.1. $l = 1$ dipole

COBE determined the dipole amplitude is 3.353 ± 0.024 mK in the direction $(l, b) = (264.26° \pm 0.33°, 48.22° \pm 0.13°)$, where l is Galactic longitude and b is Galactic latitude (Bennett et al. 1996). This dipole was subtracted from the *WMAP* data during processing. Examination of the *WMAP* maps allow for the determination of a residual dipole, and thus an improvement over the *COBE* value. Note that this does not have any effect on *WMAP* calibration, which is based on the Earth's velocity modulation of the dipole, and not on the dipole itself. The *WMAP* -determined dipole is 3.346 ± 0.017 mK in the direction $(l, b) = (263.^\circ85 \pm 0.^\circ1, 48.^\circ25 \pm 0.^\circ04)$. The uncertainty of the dipole amplitude is limited by the *WMAP* 0.5% calibration uncertainty, which will improve with time.

7.2. $l = 2$ quadrupole

The quadrupole is the $l = 2$ term of the spectrum $\Delta T_l^2 = l(l+1)C_l/2\pi$, i.e. $\Delta T_{l=2}^2 = (3/\pi)C_{l=2}$. Alternately, the quadrupole amplitude can be expressed as $Q_{rms} = \sqrt{(5/4\pi)\, C_{l=2}} = \sqrt{5/12}\, \Delta T_{l=2}$. The 4-year *COBE* quadrupole is

$Q_{rms} = 10^{+7}_{-4}$ μK with the peak of the likelihood in the range 6.9 μK $< Q_{rms} <$ 10 μK, as shown in Figure 1 of Hinshaw et al. (1996a).

The *WMAP* quadrupole, $Q_{rms} = 8 \pm 2$ μK or $\Delta T_2^2 = 154 \pm 70$ μK^2, is consistent with *COBE* but with tighter limits because of better measurements and understanding of foregrounds. The foreground level is still the leading uncertainty. (The small kinematic quadrupole is not removed from the maps nor accounted for in this analysis.) The quadrupole value is low compared with values predicted by ΛCDM models that fit the rest of the power spectrum. ΛCDM models, in particular, tend to predict relatively high quadrupole values due to the enhanced, Λ-driven, integrated Sachs-Wolfe effect.

7.3. n-poles

A central part of the task of computing multipole information from the maps is the evaluation and propagation of errors and uncertainties. This largely involves arriving at an adequate representation of the Fisher matrix, which is the inverse covariance matrix of the data. The Fisher matrix must take into account mode-coupling from the sky cut, beam (window function) uncertainties, and noise properties. The fact that the *WMAP* data use a nearly azimuthally symmetric cut, and have a nearly diagonal pixel-pixel covariance, greatly simplifies the evaluation of the Fisher matrix.

Two approaches to computing the angular power spectrum have been used by Hinshaw et al. (2003b): a quadratic estimation based on Hivon et al. (2002); and a maximum likelihood estimate based on Oh et al. (1999). The quadratic estimator is used in the final *WMAP* spectrum analyses, while the maximum likelihood technique is used as a cross-check.

The K-band and Ka-band beam sizes are large enough that these bands are not used for CMB analysis since they have the most foreground contamination and probe the region in l-space that is cosmic variance limited by the measurements at the other bands. These bands are invaluable, however, as monitors of Galactic emission. The two Q-band, two V-band, and four W-band differencing assemblies are the source of the prime CMB data. The matrix of auto- and cross-correlations between the eight Q-, V-, and W-band differencing assemblies has eight diagonal (auto-correlations) and 28 unique off-diagonal elements (cross-correlations). Since auto-correlations are difficult to assess due to the noise bias (see equation 8), we included only the 28 unique off-diagonal (cross-correlations) in the *WMAP* power spectrum analysis. In dropping the auto-correlations, each of which has twice the noise variance of a cross-correlation, we lose only $1 - \sqrt{56/(56+8)} = 6\%$ of the ideally achievable signal-to-noise ratio. In Hinshaw et al. (2003b), we show that the power spectrum computed from the auto-correlation data is consistent with the angular power spectrum from the cross-correlation data. We anticipate using the auto-correlation data in future analyses.

The cross-power spectrum from the 28 pairs is considered in four l ranges. For $l \leq 100$ we use uniform pixel weighting of only V- and W-band data. This reduces the Galactic contamination where measurement errors are well below the cosmic variance. For $100 < l \leq 200$ we use uniform pixel weighting of the combined 28 pairs. For $200 < l \leq 450$ all 28 cross-power pairs are used with a transitional pixel weighting. For $l > 450$ all 28 pairs are used with inverse noise weighting. Our Monte Carlo simulations show that this is a nearly optimal scheme.

The angular power spectrum is shown for the *WMAP* data in Figure 12. The *WMAP* power spectrum agrees closely with *COBE* at the largest angular scales, and with CBI and ACBAR at the finer angular scales. We highlight the CBI and ACBAR results because they are a useful complement to *WMAP* at the smaller angular scales. The acoustic pattern is obvious. Page et al. (2003b) find that the first acoustic peak is $\Delta T_l = 74.7 \pm 0.5$ μK at $l = 220.1 \pm 0.8$. The trough following this peak is 41.0 ± 0.5 μK at $l = 411.7 \pm 3.5$ and the second peak is 48.8 ± 0.9 μK at $l = 546 \pm 10$.

ΛCDM models predict enhanced large angle power due to the integrated Sachs-Wolfe effect. The *WMAP* and

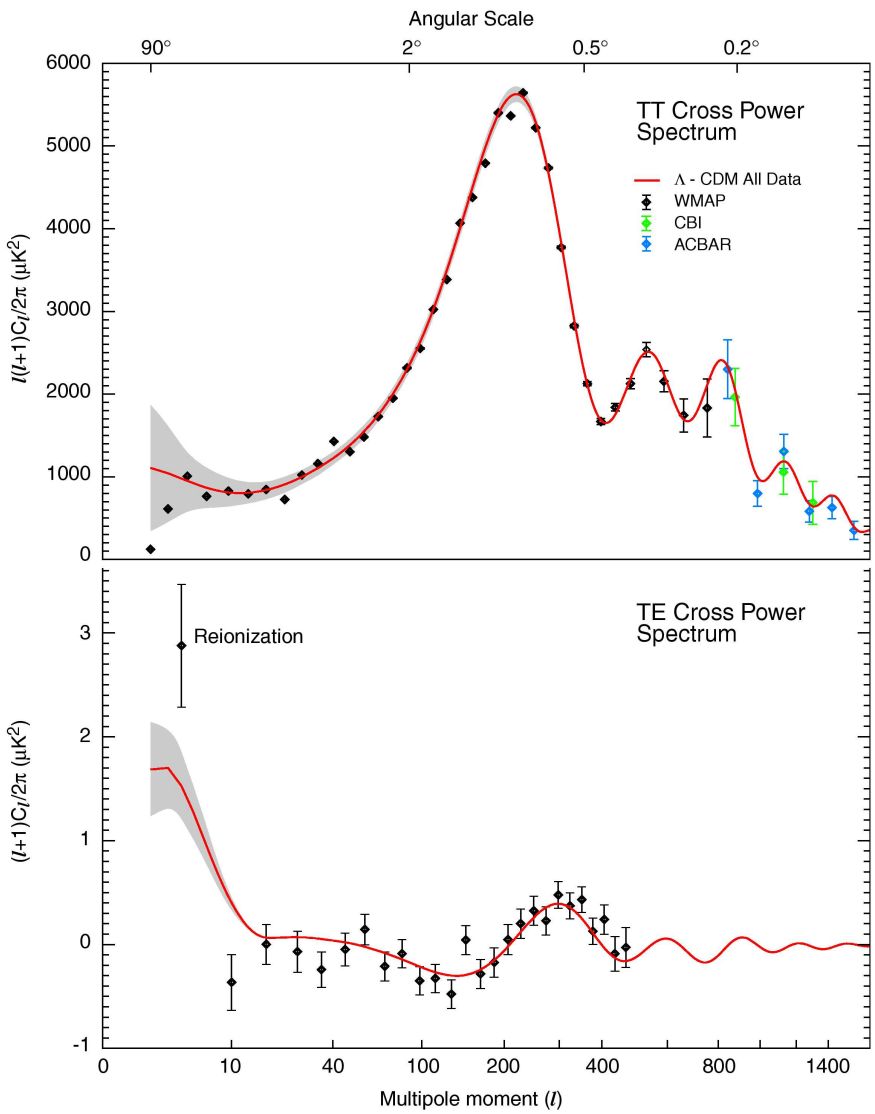

Fig. 12.— The *WMAP* angular power spectrum. (*top*:) The *WMAP* temperature (TT) results are consistent with the ACBAR and CBI measurements, as shown. The TT angular power spectrum is now highly constrained. Our best fit running index ΛCDM model is shown. The grey band represents the cosmic variance expected for that model. The quadrupole has a surprisingly low amplitude. Also, there are excursions from a smooth spectrum (e.g., at $\ell \approx 40$ and $\ell \approx 210$) that are only slightly larger than expected statistically. While intriguing, they may result from a combination of cosmic variance, subdominant astrophysical processes, and small effects from approximations made for this first year data analysis (Hinshaw et al. 2003b). We do not attach cosmological significance to them at present. More integration time and more detailed analyses are needed. (*bottom*:) The temperature-polarization (TE) cross-power spectrum, $(l+1)C_l/2\pi$. (Note that this is *not* multiplied by the additional factor of l.) The peak in the TE spectrum near $l \sim 300$ is out of phase with the TT power spectrum, as predicted for adiabatic initial conditions. The antipeak in the TE spectrum near $l \sim 150$ is evidence for superhorizon modes at decoupling, as predicted by inflationary models.

COBE data, on the other hand, have the opposite trend. The conflict is also seen clearly in the correlation function, $C(\theta)$, shown in Figure 13. The *WMAP* correlation function is computed on the Kp0 cut sky, and the *COBE* correlation function is computed on the "custom cut" sky (Bennett et al. 1996). The best-fit ΛCDM model is shown with a grey band indicating one standard deviation as determined by Monte Carlo simulations.

The lower two plots in Figure 13 display the correlation function of the difference between the *COBE*-DMR and *WMAP* maps with a $|b| = 10°$ Galactic plane cut. A synthesis of the *WMAP* Q- and V-band maps was made to approximate a 53 GHz map to compare with the *COBE*-DMR 53 GHz map. The *COBE*-DMR 90 GHz map is compared directly, without corrections, to the *WMAP* W-band map. These plots emphasize the consistency of the *WMAP* and *COBE* measurements. The slightly higher than expected deviations at 53 GHz are likely to be due to Galactic contamination, arising from outside the cut regions and from the construction of the synthesized *WMAP* 53 GHz map.

Since a correlation plot emphasizes the very low l power, the discrepancy between the model and *WMAP* data illustrates that there is surprisingly little anisotropy power in the *WMAP* (and *COBE*) maps at large separation. This result is generically true for ΛCDM models, independent of the exact parameters of the model. *There is very little large scale CMB anisotropy power in our sky. This fact, first seen by COBE is confirmed by WMAP.* The probability of so little $C(\theta > 60°)$ anisotropy power is $\sim 2 \times 10^{-3}$, given the best-fit ΛCDM model. The lack of power is seen both in $C(\theta)$ and the behavior of the low order ($l = 2, 3, 4,$ and 5) multipoles.

8. CMB POLARIZATION & THE DETECTION OF REIONIZATION

Each differencing assembly measures the sky in two orthogonal linear polarizations. As the Observatory spins, precesses, and orbits the Sun, the instrument observes the sky over a range of polarization angles. The range of angles observed is neither complete nor uniform, but it is sufficient to provide valuable new CMB polarization results.

We express polarization in term of the standard I, Q, and U Stokes parameters, in units of thermodynamic temperature. Polarization coordinates are not rotationally invariant so a coordinate system is defined by Kogut et al. (2003) for expressing information. By appropriate summing and differencing of the time-ordered-data from the pairs of corresponding radiometers, we iteratively make maps in unpolarized intensity, I, and in each polarized component, Q and U (Hinshaw et al. 2003b). The Q and U maps not only have much lower signal-to-noise than the I maps, but they are more susceptible to systematic errors since the differencing between radiometer outputs occurs on the ground, not in the front-end of the radiometers.

The U polarization maps are expected to be most affected by systematic errors. This is due to the orientation of the observed polarization angles relative to the spin axis of the Observatory, causing systematics not fixed on the sky to preferentially go into the U map.

Taurus A, an extremely strong source in the *WMAP* bands, is polarized and its polarization amplitude and direction are known (Flett & Henderson 1979). Polarization measurements from *WMAP* are consistent with previous observations of Taurus A, providing a useful check on the operation of the *WMAP* hardware and software. However, the polarization systematic errors have not yet been fully quantified. We chose to release the I data and results as soon as possible, rather than postpone their publication and release until the systematic measurement errors of the Q and U data are fully assessed. All data, including the Q and U maps will be released when the characterization of their instrumental signatures are complete. Results of temperature-polarization correlations between the I and Q maps, i.e. TE correlations, are much less sensitive to systematic effects than polarization signals alone, so we are able to report those results.

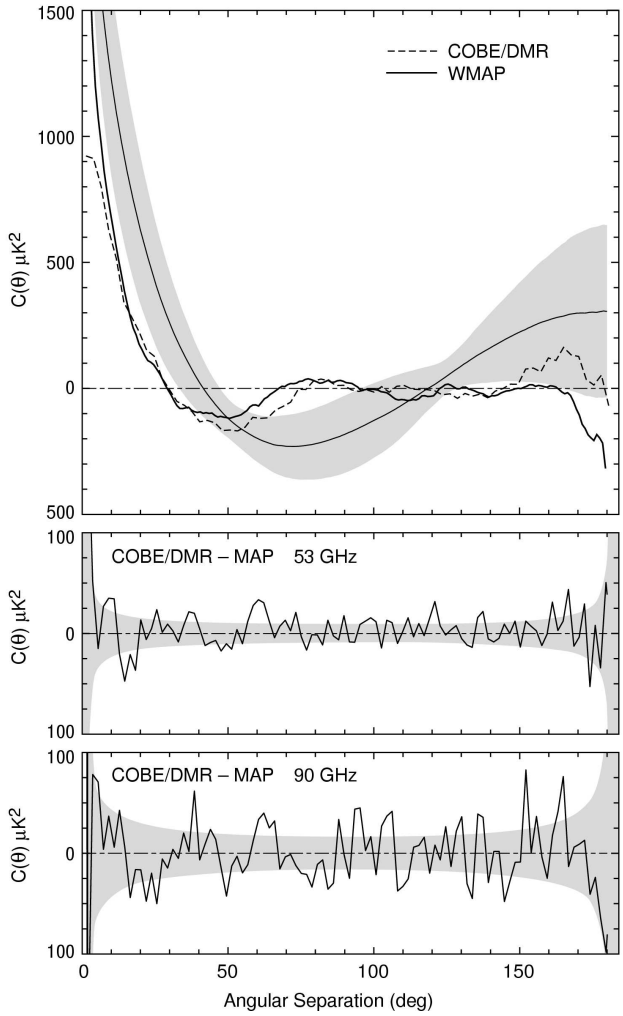

Fig. 13.— *(top):* CMB temperature correlation function of the *WMAP* and *COBE* data. The *WMAP* correlation function is computed using the Kp0 cut sky, and the *COBE* correlation function is computed using the "custom cut" sky. The running index ΛCDM model that is fit to the power spectrum is shown with a Monte Carlo determined grey band indicating one standard deviation. The model is, overall, an excellent fit to the *WMAP* power spectrum. However, a correlation plot emphasizes the low l power. The discrepancy between the model and data illustrates that there is surprisingly little anisotropy power in the *WMAP* and *COBE* maps at large angles. *(bottom):* The lower two plots display the correlation function of the difference between the *COBE*-DMR and *WMAP* maps with a $|b| = 10°$ Galactic plane cut. A synthesis of the *WMAP* Q and V band maps was made to approximate a 53 GHz-like map to compare with the *COBE*-DMR 53 GHz map. The *COBE*-DMR 90 GHz map is compared directly, without corrections, to the *WMAP* W-band map. These plot emphasize the consistency of the *WMAP* and *COBE* measurements. The slightly higher than expected deviations at 53 GHz are likely to be due to Galactic contamination, arising from outside the cut regions and from the construction of the synthesized *WMAP* 53 GHz map.

Figure 12 shows the temperature-polarization (TE) cross power spectrum. Kogut et al. (2003) report a detection of TE correlations on both large angular scales (from reionization) and on small scales (from the adiabatic fluctuations). The TE power spectrum, shown in Figure 12, is discussed in detail by Kogut et al. (2003). In the TE angular power spectrum the antipeak is $-35 \pm 9\ \mu\mathrm{K}^2$ at $l = 137 \pm 9$ and the peak is $105 \pm 18\ \mu\mathrm{K}^2$ at $l = 329 \pm 19$ (Page et al. 2003b).

The detection of the reionization of the universe corresponds to an optical depth $\tau = 0.17 \pm 0.04$ ($0.09 \leq \tau \leq 0.28$ at 95% confidence). Although *WMAP* measures the integrated optical depth, the epoch and redshift of reionization can be derived from the integral optical depth within the context of a model of the reionization process. A single instantaneous step function from $\tau = 0$ to a steady fixed value of τ is physically unlikely. For more likely models, Kogut et al. (2003) conclude that the redshift of reionization is $z_r = 20^{+10}_{-9}$ (95% CL), corresponding to an epoch of reionization of $t_r = 180^{+220}_{-80}$ Myr (95% CL) after the Big Bang. Cen (2002) presents a detailed model of a reionization process and predicts an integral value of the optical depth, $\tau = 0.10 \pm 0.03$. This is low compared with the newly measured value, but would be higher and consistent if the assumed cosmological parameters in the model were adjusted to the values of the new *WMAP* best-fit parameters (see §9.1).

The measured optical depth means that reionization suppressed the acoustic peak amplitudes by $1 - e^{-2\tau} \approx 30\%$. While accounted for in our model fits (§9, below), this suppression was not accounted for in previous CMB parameter determinations. The anticorrelations observed in the TE power spectrum directly imply superhorizon fluctuations, a new result in support of inflation-like theories, as discussed in §9.3.

9. COSMOLOGICAL INTERPRETATION

In this section we summarize the cosmological intepretation of *WMAP* first year results, which are discussed in more detail by Spergel et al. (2003), Peiris et al. (2003), Page et al. (2003b), and Kogut et al. (2003). The methodology used in the model fits is described by Verde et al. (2003).

Spergel et al. (2003) show that a cosmological model with a flat universe, seeded with a scale-invariant spectrum of adiabatic Gaussian fluctuations, with reionization, is an acceptable fit not only to the *WMAP* data but also to a host of astronomical data. These data are: smaller angular scale CMB anisotropy data from ACBAR (Kuo et al. 2002) and CBI (Pearson et al. 2002); the HST key project value of H_0 (Freedman et al. 2001); the accelerating Universe seen in Type Ia SNe (Riess et al. 2001); the shape and amplitude of the large scale structure seen in clusters and superclusters of galaxies (Percival et al. 2001; Verde et al. 2003); and the linear matter power spectrum seen in the Lyman α forest (Croft et al. 2002). There has been mounting evidence in the direction of this model for years (Peebles 1984; Bahcall et al. 1999). The optical depth since reionization is a new, but not surprising component of the model. The *WMAP* data establish this model as the standard model of cosmology by testing the key assumptions of the model and by enabling a precise determination of its parameters.

The *WMAP* data test several of the key tenets of the standard model. The *WMAP* detection of temperature-polarization correlations (Kogut et al. 2003) and the clear detection of acoustic peaks (Page et al. 2003b) implies that the primordial fluctuations were primarily adiabatic: the primordial ratio of dark matter/photons and the primordial ratio of baryons/photons do not vary spatially. The analysis of the *WMAP* temperature data demonstrates Gaussianity (Komatsu et al. 2003). The *WMAP* data, when combined with any one of the following three external data sets: HST Key Project measurement of H_0 (Freedman et al. 2001), the 2dFGRS measurement of the matter density (Percival et al. 2001; Verde et al. 2003) *or* the Type Ia supernova measurements (Riess et al. 2001) imply that the radius of curvature of the universe, $R = cH_0^{-1}|1-\Omega_{tot}|^{-1/2}$, must be very large, $\Omega_{tot} = 1.02 \pm 0.02$ and $0.99 < \Omega_{tot} < 1.05$ (95% CL). These measurements also require that the dark energy be the dominant constituent of Ω_{tot}. The *WMAP* data alone rule out the standard $\Omega_m = 1$ CDM model by $> 7\sigma$.

9.1. Best Fit Cosmological Model

While an acceptable fit, the model described above is not our best fit model. In the discussion below we concentrate on our best fit model, which adds a scale-dependent primordial spectral index. This cosmological model is a flat universe with a baryon fraction of $\Omega_b = 0.044 \pm 0.004$, a matter fraction of $\Omega_m = 0.27 \pm 0.04$, and a dark energy fraction of $\Omega_\Lambda = 0.73 \pm 0.04$, seeded with a scale-dependent spectrum of adiabatic Gaussian fluctuations. This model has $C_{l=10} = 46.0\ \mu\mathrm{K}^2$, consistent with the *COBE* measurement of $C_{l=10} = 44.4\ \mu\mathrm{K}^2$.

The *WMAP* data alone enable accurate determinations of many of the key cosmological parameters (Spergel et al. 2003). But a combination of the *WMAP* data with the *COBE* determination of the CMB temperature (Mather et al. 1999), the CBI (Pearson et al. 2002) and the ACBAR (Kuo et al. 2002) CMB measurements, and the 2dFGRS survey determination of the power spectrum of the local galaxy fluctuations (Percival et al. 2001), yields the best fit cosmological parameters listed in Table 3. Verde et al. (2003) describes our methodology for determining these parameters and Spergel et al. (2003) describes the best fit models for different combinations of data sets.

A power spectrum of primordial mass fluctuations with a scale invariant spectral index is given by $P(k) = Ak^{n_s}$ with $n_s = d\ln P/d\ln k$. Inflationary models predict a running spectral index (Kosowsky & Turner 1995), and our best fit model uses a power spectrum of primordial mass fluctuations with a scale-dependent spectral index:

$$P(k) = P(k_0)\left(\frac{k}{k_0}\right)^{n_s(k_0)+(1/2)(dn_s/d\ln k)\ln(k/k_0)}. \tag{9}$$

As in the scale-independent case, we define

$$n_s(k) \equiv \frac{d\ln P}{d\ln k}, \tag{10}$$

so

$$n_s(k) = n_s(k_0) + \frac{dn_s}{d\ln k}\ln\left(\frac{k}{k_0}\right) \tag{11}$$

(with $d^2n_s/d\ln k^2 = 0$). The definition for n_s used here includes a factor of $(1/2)$ difference from the Kosowsky & Turner (1995) definition. Peiris et al. (2003) explore the implications of this running spectral index for inflation. The best fit values of A, n_s and $dn_s/d\ln k$ are in Table 3 for $k_0 = 0.05\ \mathrm{Mpc}^{-1}$. A is the normalization parameter in CMBFAST version 4.1 with option UNNORM. The amplitude of curvature fluctuations at the horizon crossing is $|\Delta_R(k_0)|^2 = 2.95 \times 10^{-9}A$. We discuss the implications of the measured values of these parameters in §9.3 and in Peiris et al. (2003).

The *WMAP* data constrains the properties of both the dark matter and the dark energy in the following ways:

(a) The *WMAP* detection of reionization at $z \sim 20$ is incompatible with the presence of significant warm dark matter density. Since the warm dark matter moves too fast to cluster in small objects, the first objects do not form in this scenario until $z \sim 8$ (Barkana et al. 2001).

(b) The running spectral index implies a lower amplitude for mass fluctuations on the dwarf galaxy scale. Dark matter simulations of models (Ricotti 2002) find that the dark matter mass profiles depend upon the spectral index on the relevant mass scale. Thus, the shallower spectral index implied by our best fit model may solve the CDM dark matter halo profile problem (Moore et al. 1998; Spergel & Steinhardt 2000).

(c) While the *WMAP* data alone are compatible with a wide range of possible properties for the dark energy, the combination of the *WMAP* data with either the HST key project measurement of H_0, the 2dFGRS measurements of the galaxy power spectrum *or* the Type Ia supernova measurements requires that the dark energy be 73% of the total density of the Universe, and that the equation of state of the dark energy satisfy $w < -0.78$ (95% CL).

9.2. Best Fit Parameters

WMAP's measurements of the baryon density, Hubble constant, and age of the universe strengthen the cosmic consistency that underlies the Big Bang model.

ATOMIC DENSITY ($\Omega_b h^2$): *WMAP* measures the atomic density at recombination to an accuracy of 4% through the shape of the angular power spectrum, and particularly through the ratio of the heights of the first to second peak (Page et al. 2003b; Spergel et al. 2003). Our best fit value is $\Omega_b h^2 = 0.0224 \pm 0.0009$. The baryon density is also probed via abundance measurements of [D]/[H] (O'Meara et al. 2001; Pettini & Bowen 2001; D'Odorico et al. 2001). It is impressive that $\Omega_b h^2$ is the same at $z = 1089$ as measured via the CMB as it is at $z = 10^9$ from Big Bang nucleosynthesis. Thus we find cosmic consistency of the baryon density throughout cosmic time and measurement technique.

HUBBLE CONSTANT (H_0): The *WMAP* measurements of the age and $\Omega_m h^2$ yield a measurement of $H_0 = 71^{+4}_{-3}$ km s^{-1} Mpc^{-1} that is remarkably consistent with the HST Key Project value of $H_0 = 72 \pm 3 \pm 7$ km s^{-1} Mpc^{-1} (Freedman et al. 2001), but with smaller uncertainty. Recent measurements of the Hubble constant from gravitational lens timing and the Sunyaev-Zeldovich effect yield independent estimates that are generally consistent, but with larger uncertainties at present. Through a variety of measurement techniques that sample different cosmic times and distances we find cosmic consistency on H_0.

AGE OF THE UNIVERSE (t_0): The first acoustic peak in the CMB power spectrum represents a known acoustic size ($r_s = 147 \pm 2$ Mpc) at a known redshift ($z_{dec} = 1089 \pm 1$). From these, *WMAP* measures the age of the universe ($t_0 = 13.7 \pm 0.2$ Gyr) to an accuracy of $\sim 1\%$ by determining the CMB light travel time over the distance determined by the decoupling surface ($d_A = 14.0^{+0.2}_{-0.3}$ Gpc) and the geometry of the universe (i.e., flat). The age of the universe is also estimated via stars in three ways:

(i) the main sequence turn-off in globular clusters yielding a cluster age of 12 ± 1 Gyr (Reid 1997);

(ii) the temperature of the coldest white dwarfs in globular clusters yielding a cluster age of 12.7 ± 0.7 Gyr (Hansen et al. 2002), and

(iii) nucleosynthesis age dating yielding an age of 15.6 ± 4.6 Gyr (Cowan et al. 1999).

These stellar ages are all consistent with age of the universe found by *WMAP*.

MATTER DENSITY ($\Omega_m h^2$): The matter density affects the height and shape of the acoustic peaks. The baryon-to-matter ratio determines the amplitude of the acoustic wave signal and the matter-to-radiation ratio determines the epoch, z_{eq}, when the energy density of matter equals the energy density of radiation. The amplitude of the early integrated Sachs-Wolfe effect signal is sensitive to the matter-radiation equality epoch. From these effects *WMAP* measures the matter density, $\Omega_m h^2$,to an accuracy of $\sim 5\%$. Large scale structure observations measure $\Omega_m h$ through the shape of the power spectrum. When combined with estimates of h, this yields $\Omega_m h^2$. Large scale velocity field measurements yield $\Omega_m^{0.6} b^{-1}$, where b is the bias in how the galaxy power spectrum traces the matter power spectrum ($P_{\rm gal} = b^2 P(k)$). Galaxy bispectrum measurements yield b, allowing for estimates of Ω_m. From the galaxy data, Verde et al. (2002) find $\Omega_m = 0.27 \pm 0.06$, which is consistent with the *WMAP* result of $\Omega_m = 0.27 \pm 0.04$.

Cluster lensing observations yield measurements of the total mass in the cluster. X-ray measurements give both the baryonic mass and the total mass through the gravitational potential. Sunyaev-Zeldovich effect observations give a different determination of the baryonic mass in clusters. The combined X-ray and SZ measurements give a value of $\Omega_b \Omega_m^{-1} = 0.081^{+0.009}_{-0.011} h^{-1}$ (Grego et al. 2001), which is reasonably consistent with 0.17 ± 0.01 from *WMAP*.

9.3. Implications for Inflation

WMAP data tests several of the key predictions of the inflationary scenario (see Peiris et al. (2003) for further discussion):

(a) Inflation predicts that the universe is flat. As noted in §9.1 and discussed in detail in Spergel et al. (2003), the combination of *WMAP* data with either H_0, Type Ia SNe, or large scale structure data constrains $|1-\Omega_{tot}| < 0.03$.

(b) Inflation predicts Gaussian random phase fluctuations. Komatsu et al. (2003) shows that the CMB fluctuations have no detectable skewness and place strong constraints on primordial non-Gaussianity. Komatsu et al. (2003) also shows that the Minkowski functionals of the *WMAP* data are consistent with the predictions of a model with Gaussian random phase fluctuations.

(c) Inflation predicts fluctuations on scales that appear to be superhorizon scales in a Friedman-Robertson-Walker (FRW) cosmology. The *WMAP* detection of an anti-correlation between polarization and temperature fluctuations on scales of $\sim 1^\circ - 2^\circ$ (Kogut et al. 2003) confirms this prediction and rules out subhorizon causal mechanisms for generating CMB fluctuations (Peiris et al. 2003).

(d) Inflation predicts a nearly scale invariant spectrum of fluctuations, as seen by *WMAP*.

The *WMAP* data, in combination with complementary cosmological data, not only test the basic ideas of the inflationary scenario but also rule out broad classes of inflationary models, and therefore the data guide us towards a specific workable inflationary scenario. The *WMAP* data place significant constraints on r, the tensor-to-scalar ratio, n_s, the slope of the scalar fluctuations and $dn_s/d\ln k$, the scale dependence of these fluctuations. The addition of an admixture of isocurvature modes does not improve the *WMAP* model fits.

The best fit model to the combination of the *WMAP*, ACBAR, CBI, 2dFGRS and the Lyman-α forest data has a spectral index that runs from $n > 1$ on the large scales probed by *WMAP* to $n < 1$ on the small scales probed by the 2dFGRS and the Lyman-α forest data. Only a handful of inflationary models predict this behavior. The Linde & Riotto (1997) hybrid inflationary model is one example. The data, however, do not yet require $n > 1$ on large scales: our best fit model has $n_s = 1.03 \pm 0.04$ at $k = 0.002$ Mpc^{-1}.

Our analysis of inflationary models (Peiris et al. 2003) marks the beginning of precision experimental tests of specific inflationary models. With the addition of on-going *WMAP* observations and future improved analyses, *WMAP* will be able to more accurately constrain τ and hence n_s on large scales. When other CMB experiments are calibrated directly to the *WMAP* sky maps, they will provide improved measurements of the temperature angular power spectrum for $l > 700$. The upcoming release of the Sloan Digital Sky Survey (SDSS) power spectrum will provide an improved measurement of the galaxy power spectrum. The SDSS Lyman-α forest data are expected to be a significant improvement over the data used in our current analysis. Looking further towards the future, ESA's *PLANCK* mission will provide improved measurements on the CMB angular power spectrum on smaller angular scales and should be able to improve constraints on r.

10. DATA PRODUCTS

All of the *WMAP* data will be released. In addition, several ancillary and analyzed data sets are released. These include beam patterns, angular spectra, etc. Some software tools are also provided. An Explanatory Supplement provides detailed information about the *WMAP* in-flight operations and data products (Limon et al. 2003). All *WMAP*

data products are distributed through the Legacy Archive for Microwave Background Data Analysis (LAMBDA) at http://lambda.gsfc.nasa.gov. This is a new NASA data center dedicated to the rapidly growing field of microwave background data archiving and analysis.

11. SUMMARY AND CONCLUSIONS

(1) *WMAP* has produced high quality full sky maps in five widely separated frequency bands. These maps can be used to test cosmological models and serve as the primary legacy of the mission.

(2) We have characterized and placed stringent limits on systematic measurement errors. The calibration is based on the modulation of the CMB dipole, and is accurate to better than 0.5%.

(3) We have demonstrated the ability to separate the CMB anisotropy from Galactic and extragalactic foregrounds. We provide masks for this purpose. In addition, we have produced CMB maps where the Galactic signal is minimized.

(4) We have a new determination of the dipole. It is 3.346 ± 0.017 mK in the direction (l, b)= ($263.^\circ 85 \pm 0.^\circ 1$, $48.^\circ 25 \pm 0.^\circ 04$).

(5) We have a new determination of the quadrupole amplitude. It is $Q_{rms} = 8 \pm 2\ \mu$K or $\Delta T_2^2 = 154 \pm 70\ \mu\mathrm{K}^2$.

(6) We have placed tight new limits on non-Gaussianity of the CMB anisotropy. The coupling coefficient of a quadratic non-Gaussian term is limited to $-58 < f_{NL} < 134$ (95% CL) (Komatsu et al. 2003).

(7) We have produced an angular power spectrum of the anisotropy with unprecedented accuracy and precision. The power spectrum is cosmic variance limited for $l < 354$ with a signal-to-noise ratio >1 per mode to $l = 658$.

(8) We have, for the first time, observed the angular power spectrum of TE temperature-polarization correlations with sufficient accuracy and precision to place meaningful limits on cosmology.

(9) We have detected the epoch of reionization with an optical depth of $\tau = 0.17 \pm 0.04$. This implies a reionization epoch of $t_r = 180^{+220}_{-80}$ Myr (95% CL) after the Big Bang at a redshift of $z_r = 20^{+10}_{-9}$ (95% CL) for a range of ionization scenarios. This early reionization is incompatible with the presence of a significant warm dark matter density.

(10) We have fit cosmological parameters to the data. We find results that are consistent with the Big Bang theory and inflation. We find that the addition of a running spectral index, while not required, improves the fit at the $\sim 2\sigma$ level. We provide values and uncertainties for a host of parameters based on this non-power-law inflationary model. Our "best" values for cosmic parameters are given in Table 3.

(11) *WMAP* continues to collect data and is currently approved for 4 years of operations at L_2. The additional data, and more elaborate analyses, will help to further constrain models. The addition of other continuously improving CMB and large scale structure observations is essential for progress towards the ultimate goal of a complete understanding of the global properties of the universe.

The *WMAP* mission is made possible by the support of the Office of Space Sciences at NASA Headquarters and by the hard and capable work of scores of scientists, engineers, technicians, machinists, data analysts, budget analysts, managers, administrative staff, and reviewers. We are grateful to the National Radio Astronomy Observatory, which designed and produced the HEMT amplifiers that made *WMAP* possible. We are grateful to A. Riess for providing the likelihood surfaces for the supernova data. D. Finkbeiner supplied us with his full sky composite map of Hα emission in advance of publication. LV is supported by NASA through a Chandra Fellowship issued by the Chandra

X-ray Observatory Center, operated by the Smithsonian Astrophysical Observatory. ML and GT are supported by the National Research Council.

REFERENCES

Bahcall, N. A., Ostriker, J. P., Perlmutter, S., & Steinhardt, P. J. 1999, Science, 284, 1481

Baker, J. C., Grainge, K., Hobson, M. P., Jones, M. E., Kneissl, R., Lasenby, A. N., O'Sullivan, C. M. M., Pooley, G., Rocha, G., Saunders, R., Scott, P. F., & Waldram, E. M. 1999, MNRAS, 308, 1173

Barkana, R., Haiman, Z., & Ostriker, J. P. 2001, ApJ, 558, 482

Barnes, C., Limon, M., Page, L., Bennett, C., Bradley, S., Halpern, M., Hinshaw, G., Jarosik, N., Jones, W., Kogut, A., Meyer, S., Motrunich, O., Tucker, G., Wilkinson, D., & Wollack, E. 2002, ApJS, 143, 567

Barnes, C. et al. 2003, ApJ, submitted

Bennett, C. L., Banday, A. J., Górski, K. M., Hinshaw, G., Jackson, P., Keegstra, P., Kogut, A., Smoot, G. F., Wilkinson, D. T., & Wright, E. L. 1996, ApJ, 464, L1

Bennett, C. L., Bay, M., Halpern, M., Hinshaw, G., Jackson, C., Jarosik, N., Kogut, A., Limon, M., Meyer, S. S., Page, L., Spergel, D. N., Tucker, G. S., Wilkinson, D. T., Wollack, E., & Wright, E. L. 2003a, ApJ, 583, 1

Bennett, C. L., Halpern, M., Hinshaw, G., Jarosik, N., Kogut, A., Limon, M., Meyer, S. S., Page, L., Spergel, D. N., Tucker, G. S., Wollack, E., Wright, E. L., Barnes, C., Greason, M., Hill, R., Komatsu, E., Nolta, M., Odegard, N., Peiris, H., Verde, L., & Weiland, J. 2003b, ApJ, submitted

Bennett, C. L., Smoot, G. F., Hinshaw, G., Wright, E. L., Kogut, A., de Amici, G., Meyer, S. S., Weiss, R., Wilkinson, D. T., Gulkis, S., Janssen, M., Boggess, N. W., Cheng, E. S., Hauser, M. G., Kelsall, T., Mather, J. C., Moseley, S. H., Murdock, T. L., & Silverberg, R. F. 1992, ApJ, 396, L7

Bennett, C. L. et al. 2003c, ApJ, submitted

Benoit, A. et al. 2003, A&A, submitted (astro-ph/0210305)

Cen, R. 2002, ApJ, submitted (astro-ph/0210473)

Cheng, E. S., Cottingham, D. A., Fixsen, D. J., Goldin, A. B., Inman, C. A., Knox, L., Kowitt, M. S., Meyer, S. S., Puchalla, J. L., Ruhl, J. E., & Silverberg, R. F. 1997, ApJ, 488, L59

Coble, K. et al. 1999, ApJ, 519, L5

Cowan, J. J., Pfeiffer, B., Kratz, K.-L., Thielemann, F.-K., Sneden, C., Burles, S., Tytler, D., & Beers, T. C. 1999, ApJ, 521, 194

Croft, R. A. C., Weinberg, D. H., Bolte, M., Burles, S., Hernquist, L., Katz, N., Kirkman, D., & Tytler, D. 2002, ApJ, 581, 20

Dawson, K. S., Holzapfel, W. L., Carlstrom, J. E., Joy, M., LaRoque, S. J., & Reese, E. D. 2001, ApJ, 553, L1

de Bernardis, P., Aquilini, E., Boscaleri, A., de Petris, M., D'Andreta, G., Gervasi, M., Kreysa, E., Martinis, L., Masi, S., Palumbo, P., & Scaramuzzi, F. 1994, ApJ, 422, L33

de Oliverira-Costa, A., Devlin, M. J., Herbig, T., Miller, A. D., Netterfield, C. B., Page, L., & Tegmark, M. 1998, ApJ, 509, L77

Dennison, B., Simonetti, J. H., & Topasna, G. A. 1998, Publications of the Astronomical Society of Australia, 15, 147

Dicker, S. R., Melhuish, S. J., Davies, R. D., Gutiérrez, C. M., Rebolo, R., Harrison, D. L., Davis, R. J., Wilkinson, A., Hoyland, R. J., & Watson, R. A. 1999, MNRAS, 309, 750

D'Odorico, S., Dessauges-Zavadsky, M., & Molaro, P. 2001, A&A, 368, L21

Finkbeiner, D. P. 2003, ApJS, accepted (astro-ph/0301558)

Finkbeiner, D. P., Davis, M., & Schlegel, D. J. 1999, ApJ, 524, 867

Flett, A. M. & Henderson, C. 1979, MNRAS, 189, 867

Freedman, W. L., Madore, B. F., Gibson, B. K., Ferrarese, L., Kelson, D. D., Sakai, S., Mould, J. R., Kennicutt, R. C., Ford, H. C., Graham, J. A., Huchra, J. P., Hughes, S. M. G., Illingworth, G. D., Macri, L. M., & Stetson, P. B. 2001, ApJ, 553, 47

Ganga, K., Cheng, E., Meyer, S., & Page, L. 1993, ApJ, 410, L57

Gaustad, J. E., McCullough, P. R., Rosing, W., & Buren, D. V. 2001, PASP, 113, 1326

Górski, K. M., Banday, A. J., Bennett, C. L., Hinshaw, G., Kogut, A., Smoot, G. F., & Wright, E. L. 1996, ApJ, 464, L11

Gott, J. R. I., Park, C., Juszkiewicz, R., Bies, W. E., Bennett, D. P., Bouchet, F. R., & Stebbins, A. 1990, ApJ, 352, 1

Grainge, K. et al. 2003, MNRAS, submitted (astro-ph/0212495)

Grego, L., Carlstrom, J. E., Reese, E. D., Holder, G. P., Holzapfel, W. L., Joy, M. K., Mohr, J. J., & Patel, S. 2001, ApJ, 552, 2

Gundersen, J. O., Lim, M., Staren, J., Wuensche, C. A., Figueiredo, N., Gaier, T. C., Koch, T., Meinhold, P. R., Seiffert, M. D., Cook, G., Segale, A., & Lubin, P. M. 1995, ApJ, 443, L57

Haffner, L. M., Reynolds, R. J., Tufte, S. L., et al. 2002, in preparation

Halverson, N. W., Leitch, E. M., Pryke, C., Kovac, J., Carlstrom, J. E., Holzapfel, W. L., Dragovan, M., Cartwright, J. K., Mason, B. S., Padin, S., Pearson, T. J., Readhead, A. C. S., & Shepherd, M. C. 2002, ApJ, 568, 38

Hanany, S., Ade, P., Balbi, A., Bock, J., Borrill, J., Boscaleri, A., de Bernardis, P., Ferreira, P. G., Hristov, V. V., Jaffe, A. H., Lange, A. E., Lee, A. T., Mauskopf, P. D., Netterfield, C. B., Oh, S., Pascale, E., Rabii, B., Richards, P. L., Smoot, G. F., Stompor, R., Winant, C. D., & Wu, J. H. P. 2000, ApJ, 545, L5

Hancock, S., Gutiérrez, C. M., Davies, R. D., Lasenby, A. N., Rocha, G., Rebolo, R., Watson, R. A., & Tegmark, M. 1997, MNRAS, 289, 505

Hansen, B. M. S., Brewer, J., Fahlman, G. G., Gibson, B. K., Ibata, R., Limongi, M., Rich, R. M., Richer, H. B., Shara, M. M., & Stetson, P. B. 2002, ApJ, 574, L155

Harrison, D. L., Rubiño-Martin, J. A., Melhuish, S. J., Watson, R. A., Davies, R. D., Rebolo, R., Davis, R. J., Gutiérrez, C. M., & Macias-Perez, J. F. 2000, MNRAS, 316, L24

Haslam, C. G. T., Klein, U., Salter, C. J., Stoffel, H., Wilson, W. E., Cleary, M. N., Cooke, D. J., & Thomasson, P. 1981, A&A, 100, 209

Hinshaw, G., Banday, A. J., Bennett, C. L., Górski, K. M., Kogut, A., Smoot, G. F., & Wright, E. L. 1996a, ApJ, 464, L17

Hinshaw, G., Branday, A. J., Bennett, C. L., Górski, K. M., Kogut, A., Lineweaver, C. H., Smoot, G. F., & Wright, E. L. 1996b, ApJ, 464, L25

Hinshaw, G. F. et al. 2003a, ApJ, submitted

—. 2003b, ApJ, submitted

Hivon, E., Górski, K. M., Netterfield, C. B., Crill, B. P., Prunet, S., & Hansen, F. 2002, ApJ, 567, 2

Jarosik, N. et al. 2003a, ApJS, 145

—. 2003b, ApJ, submitted

Knox, L. & Page, L. 2000, Phys. Rev. Lett., 85, 1366

Kogut, A., Banday, A. J., Bennett, C. L., Górski, K. M., Hinshaw, G., Jackson, P. D., Keegstra, P., Lineweaver, C., Smoot, G. F., Tenorio, L., & Wright, E. L. 1996a, ApJ, 470, 653

Kogut, A., Banday, A. J., Bennett, C. L., Górski, K. M., Hinshaw, G., Smoot, G. F., & Wright, E. I. 1996b, ApJ, 464, L5

Kogut, A., Banday, A. J., Bennett, C. L., Górski, K. M., Hinshaw, G., Smoot, G. F., & Wright, E. L. 1996c, ApJ, 464, L29

Kogut, A., Smoot, G. F., Bennett, C. L., Wright, E. L., Aymon, J., de Amici, G., Hinshaw, G., Jackson, P. D., Kaita, E., Keegstra, P., Lineweaver, C., Loewenstein, K., Rokke, L., Tenorio, L., Boggess, N. W., Cheng, E. S., Gulkis, S., Hauser, M. G., Janssen, M. A., Kelsall, T., Mather, J. C., Meyer, S., Moseley, S. H., Murdock, T. L., Shafer, R. A., Silverberg, R. F., Weiss, R., & Wilkinson, D. T. 1992, ApJ, 401, 1

Kogut, A. et al. 2003, ApJ, submitted

Komatsu, E. & Spergel, D. N. 2001, Phys. Rev. D, 63, 63002

Komatsu, E. et al. 2003, ApJ, submitted

Kosowsky, A. & Turner, M. S. 1995, Phys. Rev. D, 52, 1739

Kovac, J. et al. 2002, ApJ, astro-ph/0209478

Kuo, C. L. et al. 2002, ApJ, astro-ph/0212289

Leitch, E. M., Readhead, A. C. S., Pearson, T. J., Myers, S. T., Gulkis, S., & Lawrence, C. R. 2000, ApJ, 532, 37

Limon, M., Wollack, E., Bennett, C. L., Halpern, M., Hinshaw, G., Jarosik, N., Kogut, A., Meyer, S. S., Page, L., Spergel, D. N., Tucker, G. S., Wright, E. L., Barnes, C., Greason, M., Hill, R., Komatsu, E., Nolta, M., Odegard, N., Peiris, H., Verde, L., & Weiland, J. 2003, unknown

Linde, A. D. & Riotto, A. 1997, Phys. Rev., D56, 1841

Mather, J. C., Cheng, E. S., Eplee, R. E., Isaacman, R. B., Meyer, S. S., Shafer, R. A., Weiss, R., Wright, E. L., Bennett, C. L., Boggess, N. W., Dwek, E., Gulkis, S., Hauser, M. G., Janssen, M., Kelsall, T., Lubin, P. M., Moseley, S. H., Murdock, T. L., Silverberg, R. F., Smoot, G. F., & Wilkinson, D. T. 1990, ApJ, 354, L37

Mather, J. C., Fixsen, D. J., Shafer, R. A., Mosier, C., & Wilkinson, D. T. 1999, ApJ, 512, 511

Mauskopf, P. D., Ade, P. A. R., de Bernardis, P., Bock, J. J., Borrill, J., Boscaleri, A., Crill, B. P., DeGasperis, G., De Troia, G., Farese, P., Ferreira, P. G., Ganga, K., Giacometti, M., Hanany, S., Hristov, V. V., Iacoangeli, A., Jaffe, A. H., Lange, A. E., Lee, A. T., Masi, S., Melchiorri, A., Melchiorri, F., Miglio, L., Montroy, T., Netterfield, C. B., Pascale, E., Piacentini, F., Richards, P. L., Romeo, G., Ruhl, J. E., Scannapieco, E., Scaramuzzi, F., Stompor, R., & Vittorio, N. 2000, ApJ, 536, L59

Miller, A. D. et al. 1999, ApJ, 524, L1

Minkowski, H. 1903, Mathematische Annalen, 57, 447

Moore, B., Governato, F., Quinn, T., Stadel, J., & Lake, G. 1998, ApJ, 499, L5+

Myers, S. T., Readhead, A. C. S., & Lawrence, C. R. 1993, ApJ, 405, 8

Netterfield, C. B., Devlin, M. J., Jarosik, N., Page, L., & Wollack, E. J. 1997, ApJ, 474, 47

Oh, S. P., Spergel, D. N., & Hinshaw, G. 1999, ApJ, 510, 551

O'Meara, J. M., Tytler, D., Kirkman, D., Suzuki, N., Prochaska, J. X., Lubin, D., & Wolfe, A. M. 2001, ApJ, 552, 718

Padin, S., Cartwright, J. K., Mason, B. S., Pearson, T. J., Readhead, A. C. S., Shepherd, M. C., Sievers, J., Udomprasert, P. S., Holzapfel, W. L., Myers, S. T., Carlstrom, J. E., Leitch, E. M., Joy, M., Bronfman, L., & May, J. 2001, ApJ, 549, L1

Page, L. et al. 2003a, ApJ, submitted

—. 2003b, ApJ, submitted

—. 2003c, ApJ, 585, in press

Pearson, T. J., Mason, B. S., Readhead, A. C. S., Shepherd, M. C., Sievers, J. L., Udomprasert, P. S., Cartwright, J. K., Farmer, A. J., Padin, S., Myers, S. T., Bond, J. R., Contaldi, C. R., Pen, U.-L., Prunet, S., Pogosyan, D., Carlstrom, J. E., Kovac, J., Leitch, E. M., Pryke, C., Halverson, N. W., Holzapfel, W. L., Altamirano, P., Bronfman, L., Casassus, S., May, J., & Joy, M. 2002, ApJ, submitted (astro-ph/0205388)

Peebles, P. J. E. 1984, ApJ, 284, 439

Peiris, H. et al. 2003, ApJ, submitted

Penzias, A. A. & Wilson, R. W. 1965, ApJ, 142, 419

Percival, W. J., Baugh, C. M., Bland-Hawthorn, J., Bridges, T., Cannon, R., Cole, S., Colless, M., Collins, C., Couch, W., Dalton, G., De Propris, R., Driver, S. P., Efstathiou, G., Ellis, R. S., Frenk, C. S., Glazebrook, K., Jackson, C., Lahav, O., Lewis, I., Lumsden, S., Maddox, S., Moody, S., Norberg, P., Peacock, J. A., Peterson, B. A., Sutherland, W., & Taylor, K. 2001, MNRAS, 327, 1297

Peterson, J. B., Griffin, G. S., Newcomb, M. G., Alvarez, D. L., Cantalupo, C. M., Morgan, D., Miller, K. W., Ganga, K., Pernic, D., & Thoma, M. 2000, ApJ, 532, L83

Pettini, M. & Bowen, D. V. 2001, ApJ, 560, 41

Piccirillo, L., Femenía, B., Kachwala, N., Rebolo, R., Limon, M., Gutiérrez, C. M., Nicholas, J., Schaefer, R. K., & Watson, R. A. 1997, ApJ, 475, L77

Reid, I. N. 1997, AJ, 114, 161

Reynolds, R. J., Haffner, L. M., & Madsen, G. J. 2002, in ASP Conf. Ser. 282, in press; ed. M. Rosado, L. Binette, L. Arias

Ricotti, M. 2002, astro-ph/0212146

Riess, A. G., Nugent, P. E., Gilliland, R. L., Schmidt, B. P., Tonry, J., Dickinson, M., Thompson, R. I., Budavári, T. . S., Evans, A. S., Filippenko, A. V., Livio, M., Sanders, D. B., Shapley, A. E., Spinrad, H., Steidel, C. C., Stern, D., Surace, J., & Veilleux, S. 2001, ApJ, 560, 49

Romeo, G., Ali, S., Femenía, B., Limon, M., Piccirillo, L., Rebolo, R., & Schaefer, R. 2001, ApJ, 548, L1

Ruhl, J. E. et al. 2003, ApJ, submitted (astro-ph/0212229)

Schlegel, D. J., Finkbeiner, D. P., & Davis, M. 1998, ApJ, 500, 525

Smoot, G. F., Bennett, C. L., Kogut, A., Wright, E. L., Aymon, J., Boggess, N. W., Cheng, E. S., de Amici, G., Gulkis, S., Hauser, M. G., Hinshaw, G., Jackson, P. D., Janssen, M., Kaita, E., Kelsall, T., Keegstra, P., Lineweaver, C., Loewenstein, K., Lubin, P., Mather, J., Meyer, S. S., Moseley, S. H., Murdock, T., Rokke, L., Silverberg, R. F., Tenorio, L., Weiss, R., & Wilkinson, D. T. 1992, ApJ, 396, L1

Spergel, D. N. & Steinhardt, P. J. 2000, Phys. Rev. Lett., 84, 3760

Spergel, D. N. et al. 2003, ApJ, submitted

Tucker, G. S., Griffin, G. S., Nguyen, H. T., & Peterson, J. B. 1993, ApJ, 419, L45+

Tucker, G. S., Gush, H. P., Halpern, M., Shinkoda, I., & Towlson, W. 1997, ApJ, 475, L73

Verde, L., Heavens, A. F., Percival, W. J., Matarrese, S., Baugh, C. M., Bland-Hawthorn, J., Bridges, T., Cannon, R., Cole, S., Colless, M., Collins, C., Couch, W., Dalton, G., De Propris, R., Driver, S. P., Efstathiou, G., Ellis, R. S., Frenk, C. S., Glazebrook, K., Jackson, C., Lahav, O., Lewis, I., Lumsden, S., Maddox, S., Madgwick, D., Norberg, P., Peacock, J. A., Peterson, B. A., Sutherland, W., & Taylor, K. 2002, MNRAS, 335, 432

Verde, L. et al. 2003, ApJ, submitted

Wilson, G. W., Knox, L., Dodelson, S., Coble, K., Cheng, E. S., Cottingham, D. A., Fixsen, D. J., Goldin, A. B., Inman, C. A., Kowitt, M. S., Meyer, S. S., Page, L. A., Puchalla, J. L., Ruhl, J. E., & Silverberg, R. F. 2000, ApJ, 532, 57

Wright, E. L., Bennett, C. L., Górski, K., Hinshaw, G., & Smoot, G. F. 1996a, ApJ, 464, L21

Wright, E. L., Hinshaw, G., & Bennett, C. L. 1996b, ApJ, 458, L53

Wright, E. L., Meyer, S. S., Bennett, C. L., Boggess, N. W., Cheng, E. S., Hauser, M. G., Kogut, A., Lineweaver, C., Mather, J. C., Smoot, G. F., Weiss, R., Gulkis, S., Hinshaw, G., Janssen, M., Kelsall, T., Lubin, P. M., Moseley, S. H., Murdock, T. L., Shafer, R. A., Silverberg, R. F., & Wilkinson, D. T. 1992, ApJ, 396, L13

This preprint was prepared with the AAS LaTeX macros v5.0.

Table 2. Data Flagging Summary

Category	K-Band	Ka-Band	Q-Band	V-Band	W-Band
Rejected or Lost Data					
Lost Data (%)	0.27	0.27	0.27	0.27	0.27
Spacecraft thermal change (%)	0.87	0.87	0.87	0.87	0.87
Gain or baseline step (%)	0.00	0.13	0.12	0.00	0.22
Total Lost or Bad Data (%)	1.04	1.27	1.26	1.14	1.36
Data Not Used in Maps					
Planet flag (%)	0.11	0.11	0.11	0.11	0.11

Table 3. "Best" Cosmological Parameters

Description	Symbol	Value	+ uncertainty	− uncertainty
Total density	Ω_{tot}	1.02	0.02	0.02
Equation of state of quintessence	w	< -0.78	95% CL	—
Dark energy density	Ω_Λ	0.73	0.04	0.04
Baryon density	$\Omega_b h^2$	0.0224	0.0009	0.0009
Baryon density	Ω_b	0.044	0.004	0.004
Baryon density (cm^{-3})	n_b	2.5×10^{-7}	0.1×10^{-7}	0.1×10^{-7}
Matter density	$\Omega_m h^2$	0.135	0.008	0.009
Matter density	Ω_m	0.27	0.04	0.04
Light neutrino density	$\Omega_\nu h^2$	< 0.0076	95% CL	—
CMB temperature (K)[a]	$T_{\rm cmb}$	2.725	0.002	0.002
CMB photon density (cm^{-3})[b]	n_γ	410.4	0.9	0.9
Baryon-to-photon ratio	η	6.1×10^{-10}	0.3×10^{-10}	0.2×10^{-10}
Baryon-to-matter ratio	$\Omega_b \Omega_m^{-1}$	0.17	0.01	0.01
Fluctuation amplitude in $8h^{-1}$ Mpc spheres	σ_8	0.84	0.04	0.04
Low-z cluster abundance scaling	$\sigma_8 \Omega_m^{0.5}$	0.44	0.04	0.05
Power spectrum normalization (at $k_0 = 0.05$ Mpc^{-1})[c]	A	0.833	0.086	0.083
Scalar spectral index (at $k_0 = 0.05$ Mpc^{-1})[c]	n_s	0.93	0.03	0.03
Running index slope (at $k_0 = 0.05$ Mpc^{-1})[c]	$dn_s/d\ln k$	–0.031	0.016	0.018
Tensor-to-scalar ratio (at $k_0 = 0.002$ Mpc^{-1})	r	< 0.71	95% CL	—
Redshift of decoupling	z_{dec}	1089	1	1
Thickness of decoupling (FWHM)	Δz_{dec}	195	2	2
Hubble constant	h	0.71	0.04	0.03
Age of universe (Gyr)	t_0	13.7	0.2	0.2
Age at decoupling (kyr)	t_{dec}	379	8	7
Age at reionization (Myr, 95% CL))	t_r	180	220	80
Decoupling time interval (kyr)	Δt_{dec}	118	3	2
Redshift of matter-energy equality	z_{eq}	3233	194	210
Reionization optical depth	τ	0.17	0.04	0.04
Redshift of reionization (95% CL)	z_r	20	10	9
Sound horizon at decoupling (°)	θ_A	0.598	0.002	0.002
Angular diameter distance to decoupling (Gpc)	d_A	14.0	0.2	0.3
Acoustic scale[d]	ℓ_A	301	1	1
Sound horizon at decoupling (Mpc)[d]	r_s	147	2	2

[a]from *COBE* (Mather et al. 1999)

[b]derived from *COBE* (Mather et al. 1999)

[c]$l_{eff} \approx 700$

[d]$\ell_A \equiv \pi \theta_A^{-1} \quad \theta_A \equiv r_s\, d_a^{-1}$